This is the peer reviewd version of the followng article:

Finite-element modeling of neuromodulation via controlled delivery of potassium ions using conductive polymer-coated microelectrodes / Verardo, C., Mele, L.J., Selmi, L., Palestri, P.. - In: JOURNAL OF NEURAL ENGINEERING. - ISSN 1741-2552. - 21:2(2024), pp. 1-18. [10.1088/1741-2552/ad2581]

*Terms of use:*

The terms and conditions for the reuse of this version of the manuscript are specified in the publishing policy. For all terms of use and more information see the publisher's website.

14/11/2026 06:11

(Article begins on next page)

# Finite-element modeling of neuromodulation via controlled delivery of potassium ions using conductive polymer-coated microelectrodes

**Claudio Verardo**[*,1,3], **Leandro Julian Mele**[*,1,4], **Luca Selmi**[2], **Pierpaolo Palestri**[1,2]

[1] Polytechnic Department of Engineering and Architecture, Università degli Studi di Udine, Udine, Italy

[2] Department of Engineering "Enzo Ferrari", Università degli Studi di Modena e Reggio Emilia, Modena, Italy

[3] BioRobotics Institute and Department of Excellence in Robotics and AI, Scuola Superiore Sant'Anna, Pisa, Italy

[4] Department of Materials Science and Engineering, Stanford University, Stanford, United States of America

[*] The authors contributed equally to the work.

E-mail: pierpaolo.palestri@uniud.it

**Abstract.** *Objective.* The controlled delivery of potassium is an interesting neuromodulation modality, being potassium ions involved in shaping neuron excitability, synaptic transmission, network synchronization, and playing a key role in pathological conditions like epilepsy and spreading depression. Despite many successful examples of pre-clinical devices able to influence the extracellular potassium concentration, computational frameworks capturing the corresponding impact on neuronal activity are still missing. *Approach.* We present a finite-element model describing a PEDOT:PSS-coated microelectrode (herein, simply *ionic actuator*) able to release potassium and thus modulate the activity of a cortical neuron in an *in-vitro*-like setting. The dynamics of ions in the ionic actuator, the neural membrane, and the cellular fluids are solved self-consistently. *Main results.* We showcase the capability of the model to describe on a physical basis the modulation of the intrinsic excitability of the cell and of the synaptic transmission following the electro-ionic stimulation produced by the actuator. We consider three case studies for the ionic actuator with different levels of selectivity to potassium: ideal selectivity, no selectivity, and selectivity achieved by embedding ionophores in the polymer. *Significance.* This work is the first step toward a comprehensive computational framework aimed to investigate novel neuromodulation devices targeting specific ionic species, as well as to optimize their design and performance, in terms of the induced modulation of neural activity.

## 1. Introduction

Extracellular potassium is a crucial modulator of neuronal activity [1], [2]. An increase in its concentration [$K^+$] lowers the outward $K^+$ fluxes in the ion channels, thereby depolarizing the membrane potential and increasing the intrinsic excitability of the cell [3]. As a result of depolarization, synaptic transmission at excitatory synapses is facilitated, since the postsynaptic current at the glutamatergic receptors is enhanced

and the release of neurotransmitters is promoted by a major presynaptic inflow of calcium through voltage-gated $Ca^{2+}$ channels [4]–[6]. At the network level, potassium accumulation and diffusion generate non-synaptic coupling between neurons, which in turn shapes network activity and may induce synchronization [7]. Perturbations of $[K^+]$ are interesting also from a neurological perspective, since they are linked to many pathological conditions such as epilepsy [8], [9] or spreading depression [10], [11]. Therefore, the control of $[K^+]$, which we will thereafter refer to as *ionic stimulation*, is drawing attention as a possible innovative pathway toward neuromodulation [12]. This has been implemented by several novel devices, herein referred to as *ionic actuators*, capable of perturbing the extracellular concentration of potassium at spatiotemporal scales approaching those of neuron activity [13]–[15].

Ionic stimulation obtained with ionic actuators fits in the broader realm of drug-delivery devices applied to neuromodulation. A prominent class of such technology relies on the properties of conductive polymers (CPs) [16], also known as organic mixed ionic and electronic conductors (OMIECs) [17]. CP-coated electrodes can modulate the local ionic concentration upon application of an electrical stimulus which translates into the injection of holes‡ (or electrons) in the polymer backbone and is followed by the release of pre-charged cations (or anions) in the target electrolyte. The pre-charging can be achieved using the electrostatic forces provided by fixed moieties in the CP blend or when the charged drugs act as dopants [18]–[20]. In the purely electrostatic CP loading, selectivity can be achieved by adding ionophores [21]–[23], using ion-selective membranes [24] or cell membrane bilayers with specific ion-channel expressions [25]. Alternative architectures that stem from the field of iontronics [26], bypass the selectivity problem by employing multiple electrolyte reservoirs where ions/drugs are stored, delivered or drained [13]–[15]. However, this approach poses evident challenges in the design and implementation of the microfluidics, requires high voltages and is thus not easy to miniaturize.

Multiphysics computational models are pivotal to aid the design and deployment of ionic actuators as neuroengineering devices, as they reduce the need for *in-vitro*/animal studies and the prototyping cost and development time. Indeed, they allow to improve the understanding of the device operation, by providing insight into underlying phenomena not directly accessible by experiments. Moreover, they enable the investigation of large regions in the parametric space, paving the way for optimum design of the neuromodulation devices. Modeling the dynamics of ionic actuators requires an accurate description of the ions' electrodiffusion. Given the relatively large dimensions of these devices, the Poisson-Nernst-Planck (PNP) model [27] is a good candidate to capture both drift and diffusion transport mechanisms, as well as charge screening effects in the space-time domain. The PNP model can also be adapted to CPs [28], and has been employed in computational works focusing on the characterization and optimization of iontronic devices [29]–[31] or ISM-cuff electrodes [32]. Notwithstanding, to the extent of

‡ More precisely, the injection of holes is associated with the creation of polarons and bipolarons in the polymer. In this paper, we use the term *holes* to ease the discussion.

our knowledge, computational frameworks accounting for both ionic actuators and their effect on neuronal membranes are still missing in the literature. This is in contrast with other neuroengineering modalities, e.g., electrical stimulation, where similar modeling frameworks are employed [33], [34].

The main difficulty of coupling the description of ionic actuators and neuronal activity resides in the workhorse models employed in computational neuroscience: the volume conductor description of the cellular fluids [35], and the cable theory framework of membrane dynamics [36]. Indeed, the former assumes the neuron milieu to be ohmic, while the latter relies on a circuit-level description of the transmembrane fluxes. As a result, the modeled electric currents have no direct connection with the underlying ionic fluxes. This is not an issue when modeling, e.g., the electric interaction with electrodes for stimulation [33], [34] and recording [37], [38], but becomes pivotal in presence of ionic actuators (see Methods). A small body of literature applied the PNP framework to describe ionic transport phenomena occurring in nervous tissues [39]–[42], mainly focusing on the study of slow potentials and microdomains. We point out that these frameworks exploit the quasistatic approximation of Maxwell equations [35], thereby neglecting capacitive and inductive effects in the cellular fluids. Also, there exists a family of models describing ion dynamics in the nervous milieu under the assumption of only diffusive fluxes [43]–[48]. However, this is in general not justifiable for non-biological electrogenic sources like ionic actuators, since that approach neglects possible components of electric stimulation arising from ion release/uptake.

In this work, we propose the first *in-silico* framework that describes the coupled dynamics of a ionic actuator, ion transport in the intra- and extra-cellular fluids (ICF, ECF), and the electrogenic processes at the neural membrane. These models are solved in a self-consistent fashion according to the electrodiffusive level of detail. As a case study, we use a PEDOT:PSS-coated microelectrode releasing $K^+$ placed below a cortical neuron soma with dome geometry. This configuration enables us to examine how the action of the ionic actuator affects neural activity, both through the perturbation of the extracellular potassium concentration (*ionic stimulation*) and of the electrical potential (*electric stimulation*). First, we showcase the extreme cases of an ionic actuator with either ideal selectivity or no selectivity to $K^+$. In the ideal case, the sole action of the ionic actuator is sufficient to drive ionically the neuron into tonic firing or depolarization block. In the non-selective case, mainly electric stimulation is delivered since the polymer is not able to collect enough potassium from the extra-cellular fluid. Second, we study a possible functionalization of the actuator's selectivity by resorting to ionophores. Simulations show that the optimized ionic actuator enhances the neuron sensitivity to concurrent electrical stimulation as well as to facilitate excitatory synaptic transmission.

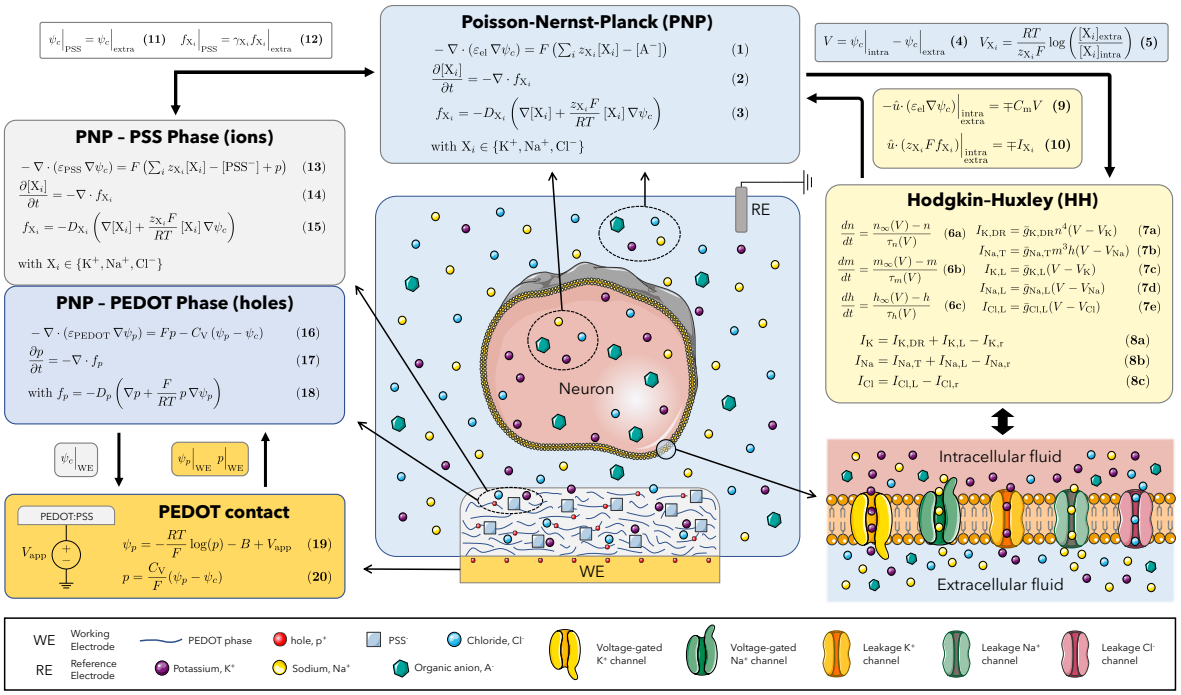



**Figure 1.** Sketch of the neuron cell (center) containing the intracellular fluid (ICF) and surrounded by the extracellular fluid (ECF), contacted by an external reference electrode (RE). Below the neuron, the CP-based ionic actuator is contacted by a metal (e.g., gold) electrode operating as working electrode (WE). The operation mechanism consists of electronic doping of the PEDOT phase that induces an ion flux pointing outwards from the CP. The equations used for each physics in the simulation domain are represented by frames placed around the main sketch. Frames are connected with arrows that indicate the coupling equations implemented in COMSOL Multiphysics. A description of the physical variables and parameters is reported in Tables S2 and S3, respectively. Part of the image is adapted from Servier Medical Art, © CC BY 3.0.

## 2. Methods

The computational framework used in this work (Fig. 1) couples the dynamics of the ionic actuator, the ICF, the ECF, and the neural membrane. It combines modeling efforts from the literature separately accounting for the CP-electrolyte interaction [28], and ion transport in cellular fluids in presence of the neural membrane's electrogenic activity [39], [43]. The simulation domains with the corresponding physics are represented by a frame and a set of equations in Fig. 1. Arrows connecting frames report the equations that couple different domains. Generalizations of the computational framework to account for ionophores and synapses are shown in Fig. 2. A description of the abbreviations, physical variables, and parameters used is reported in the supplementary materials in Tables S1, S2, and S3, respectively. The model is implemented in COMSOL Multiphysics [49] (technical details are reported in the Supplementary Note 1). In the following, we briefly describe the model equations, the reference physical and geometrical parameters, as well as the case studies examined. The model verification is addressed in the Supplementary Note 2.

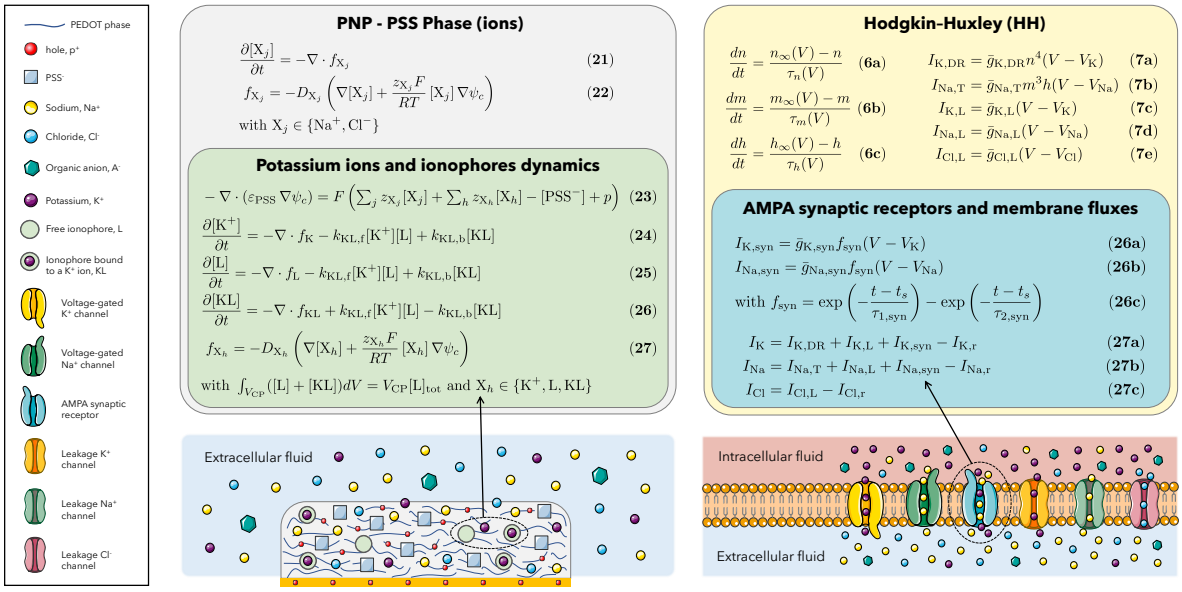



**Figure 2.** Sketch illustrating the changes made to the modeling framework shown in Fig. 1 to account for the dynamics of ionophores (left) and AMPA excitatory synapses (right). Green and blue insets highlight the new or updated equations in the PNP-PSS model of the CP (grey frame, as in Fig. 1) and the HH model of the neural membrane (yellow frame, as in Fig. 1). A description of the physical variables and parameters is reported in Tables S2 and S3, respectively. Part of the image is adapted from Servier Medical Art, © CC BY 3.0.

## *2.1. Model equations*

*2.1.1. Intra- and extra-cellular fluids* The ECF and ICF are modeled as electrolytes using the PNP equations (Eqs. 1-3). The electrostatic potential of the ions, $\psi_c$, is obtained by solving the Poisson equation (Eq. 1), which depends on the local space and time-dependent net charge density due to all the ionic species in the aqueous phase. For simplicity, we restrict the analysis to the main ionic agents responsible for the generation of action potentials (APs) at the neural membrane, namely $K^+$, $Na^+$, $Cl^-$. The bulk concentrations are taken from [43], in agreement with typical (artificial) cerebrospinal fluids [1]. A generic anion $A^-$, assumed fixed and uniformly distributed for simplicity, is added to provide electroneutrality (i.e., $[K^+]+[Na^+]-[Cl^-]-[A^-]=0$) in the bulk of the solutions. Mass conservation of each mobile species is enforced with the continuity equations (Eqs. 2). Therefore, time-dependent variations of ionic concentrations are given by drift and diffusion fluxes and described using the Nernst-Planck transport equations (Eqs. 3). Note that, Eqs. 1-3 are solved in both the extra and intracellular domains. The presence of an extracellular reference electrode (RE) is mimicked through boundary conditions in the ECF's bulk that set the electric potential to ground and the ionic concentrations to their baseline values. Since no limit on the RE's current is imposed, such boundary conditions also account for the action of a counter electrode (CE).

*2.1.2. Neural membrane* The transmembrane fluxes through ion channels are modeled using the Hodgkin-Huxley (HH) formalism (Eqs. 6-8), implemented at each mesh point of the cell membrane. The HH model of this work has been introduced in [43] and later used to describe an interneuron of the rat CA1 hippocampus [50], [51]. It includes a transient sodium current (subscript T) and a delayed rectifying potassium current (subscript DR), which are voltage-gated and responsible for the generation of APs (Eqs. 7a-b). Moreover, our implementation has a leakage current (subscript L) specific for each ion species (Eqs. 7c-e), differently to the original HH model [52]. Equation 6 collects three first-order differential equations modeling the dynamics of the gating variables for the potassium ($n$) and sodium ($m$, $h$) voltage-gated channels, which depend on the (in)activation curves $n_\infty$, $m_\infty$, $h_\infty$, and time constants $\tau_n$, $\tau_m$, $\tau_h$, respectively. Equation 8 reports the total transmembrane current density for each ion species, which depends (through Eq. 7) on the maximum conductances of the ion channels, the gating variables, and the difference between the membrane and reversal potentials (see Section 2.1.3). In order to preserve the rest potential $V_\mathrm{r}$ of the chosen HH model at the steady state, each current density in Eq. 8 is shifted by its value $I_{\mathrm{X}_i,\mathrm{r}}$ at $V_\mathrm{r}$, where $\mathrm{X}_i \in \{\mathrm{K}^+,\ \mathrm{Na}^+,\ \mathrm{Cl}^-\}$, and therefore is null under steady-state conditions. We note that alternative choices for the steady state are possible. For instance, in [39] the authors block the voltage-gated channels and let the system achieve the thermodynamic equilibrium. Nevertheless, since sub-threshold fluxes are orders of magnitude smaller than the ones that shape neural firing, these choices are expected to mildly impact the system's behavior. Since our investigations focus on temporal scales of tens to hundreds of milliseconds (see Results), we do not account for homeostatic mechanisms responsible for the regulation of ion concentration, such as ion transporters at the neural membrane or spatial buffering by glial cells [2]. The interaction of these mechanisms with ion dynamics is expected to become relevant at the scale of seconds or longer [43]–[48].

*2.1.3. Coupling HH and PNP models* The currents through ion channels are imposed as flux boundary conditions in and out of the cell (Eq. 10), according to the ion currents given by Eq. 8. The dielectric effects of the membrane are modeled as an ideal capacitor with parallel plates via a thin layer approximation. Namely, they are accounted for through boundary conditions on the electric displacement field that depends on the membrane capacitance $C_\mathrm{m}$ and the membrane potential $V$ (Eq. 9). These conditions are responsible for the electrical double layer (EDL) formation at the two sides of the membrane, and avoid the need to explicitly solve the Poisson equation in the membrane domain (as done, e.g., in [39]), thereby reducing the computational cost. The HH model extracts the membrane potential $V$ by sampling the electrostatic potential predicted by the PNP at the intra- and extra-cellular side of the neural membrane (Eq. 4). Differently from previous works [39], the runtime calculation of the reversal potentials $V_\mathrm{K}$, $V_\mathrm{Na}$, $V_\mathrm{Cl}$ is done by sampling the ionic concentrations at a distance $d_\mathrm{s}$ = 6 nm from the neural membrane, i.e., a distance 5 times larger than the Debye length [27] in the ECF and ICF (Eq. 5). This strategy is adopted to avoid distortion of the ion concentrations induced

by charge screening effects in the EDL.

*2.1.4. Ionic actuator* The ionic actuator consists of a film of conjugated polymer-polyelectrolyte blend (hereafter simply referred to conductive polymer, CP), that is, a two-phase domain where both ionic and electronic transport take place simultaneously (see Fig. 1). We consider a PEDOT:PSS blend as the reference CP and use the model proposed in [28]. According to [28], the polyelectrolyte PSS phase and the PEDOT phase can be modeled by coupling two PNP sets of equations: in the PNP of the PSS phase, the concentration of holes is added to the space charge density of the Poisson equation so that ions are electrostatically influenced by the holes' spatial distribution (see Eq. 13); differently, in the PNP of the PEDOT phase the electrostatic potential of holes, $\psi_p$, in the Poisson equation (Eq. 16) depends on $\psi_c$ in the form of a capacitive coupling, namely, through the volumetric capacitance $C_{\mathrm{V}}$ (with units of $\mathrm{F/cm^3}$). This phenomenological term quantifies the extent of entanglement between the two phases and can be seen as the result of a three-dimensional EDL [53], [54]. Mass conservation of ions and holes in their respective phase is also ensured by the continuity equations (Eqs. 14 and 17), where electrodiffusive fluxes are described with the Nernst-Planck equation (Eqs. 15 and 18). Note that, for the sake of simplicity, we do neglect reactions occurring at the CP/electrolyte interface [55], such as oxygen reduction reactions (ORRs) often seen in PEDOT:PSS CPs [56]. This phenomenon should translate into an additional faradaic current drawn by the WE when using a negative bias but should not sensibly impact the capacitive mechanism that enables the ionic injection in the extracellular fluid.

*2.1.5. Coupling between polyelectrolyte and extracellular fluid* Since polyelectrolyte and electrolyte phases are both ionic phases, the PSS/ECF interface must ensure continuity of the electrostatic potential (see Eq. 11). Fluxes of ions, however, may experience affinity changes due to, e.g., ionophores incorporated in CP [21], [22] or from ion-selective barriers [25]. For the sake of generality, we equipped our model with virtual affinity coefficients $\gamma_{\mathrm{K}}$, $\gamma_{\mathrm{Na}}$, $\gamma_{\mathrm{Cl}}$ at the PSS/ECF interface equal to either 0 or 1 (see Eq. 12) to introduce ideal selectivity of the CP to specific ions (see Section 2.2).

*2.1.6. Ionophores* While the parameters $\gamma_{\mathrm{X}_i}$, $\mathrm{X}_i \in \{\mathrm{K^+},\ \mathrm{Na^+},\ \mathrm{Cl^-}\}$, are used as phenomenological terms to induce ideal selectivity, ionophores are employed as a more realistic way to describe a selective ionic actuator [21], [22]. With respect to the ideal CP, the physics of an ionophore-containing CP (described in Fig. 2, left panel) also includes the continuity equations (Eqs. 25, 26) for the free ionophores, L, as well as the selective complexes formed with potassium ions, KL. Forward and backward reaction terms are included in these equations and the continuity equation for $\mathrm{K^+}$ ions (Eq. 24) to account for the binding and unbinding mechanisms of ionophores and potassium ions [57]. Electrodiffusive fluxes are described by the Nerst-Planck equation (Eq. 27). Note that ionophores are confined in the CP domain and can be regarded as fixed or mobile

depending on the value of their diffusivity coefficient. Moreover, in this work we assume the ionophore molecules as neutral species so that only their complexed form (positively charged) contributes to the Poisson equation (Eq. 23). The continuity equations and the electrodiffusive fluxes for $Na^+$ and $Cl^-$ are the same as in Eqs. 14-15 but, for the sake of clarity, they are also reported in Eqs. 21-22 to explicitly separate the $K^+$ dynamics.

*2.1.7. Synapses* A model of excitatory synapse (described in Fig. 2, right panel) is included in the neural membrane when testing the neuromodulation capability of the CP beyond to purely induce APs (see Section 3.4). The model is taken from [58] and accounts for the $K^+$ and $Na^+$ fluxes through an AMPA postsynaptic receptor (Eq. 26). We consider only single synaptic events for each simulation. The excitatory postsynaptic currents (EPSCs) are described with a template profile for the ion postsynaptic conductances, and are modulated by the membrane and reversal potentials. The total transmembrane currents for each ion species are updated accordingly (Eq. 27). Differently to [58], we neglect the small calcium component to avoid the additional computational cost of modeling the $Ca^{2+}$ electrodiffusion in the cellular fluids.

### *2.2. Case studies for the ionic actuator*

In the present work, we consider 3 case studies of CP with different levels of selectivity towards $K^+$ in terms of storage and release.

- *Ideally-selective CP* (isCP): $Na^+$ ions cannot enter the CP. This is accomplished by setting $\gamma_{Na} = 0$ while $\gamma_K = \gamma_{Cl} = 1$. The physical parameters of the CP are taken from the literature [28], [53], [55] and ionophores are not embedded in the CP backbone. As a result, the CP in the undoped state is pre-charged almost completely with $K^+$, which compensates the fixed moieties $PSS^-$.
- *Non-selective CP* (nsCP): the CP is permeable to all of the ions ($\gamma_{Na} = \gamma_K = \gamma_{Cl} = 1$). The physical parameters of the CP are taken from the literature [28], [53], [55] and ionophores are not embedded in the CP backbone. As a result, the CP in the undoped state is pre-charged by both $K^+$ and $Na^+$, in same proportions as in the ECF (where $[Na^+] \gg [K^+]$).
- *Ionophores-induced selective CP* (ionoCP): the CP is permeable to all of the ions as in the previous case, but it is endowed with ionophores, that enhance the proportion of $K^+$ ions inside the CP. However, their binding affinity resists to the ion release into the ECF. To get the best from this trade-off, we tailor the chemical parameters of the CP and of the ionophores by resorting to a simplified phase boundary model for the CP with ionophores and its interaction with the ECF (see Supplementary Note 3).

If not otherwise specified, we use the values reported in Table S3 for the physical parameters. For the convenience of the reader, we report in Table S4 the parameters and the correspondent values adopted to instantiate the isCP, nsCP, ionoCP case studies.

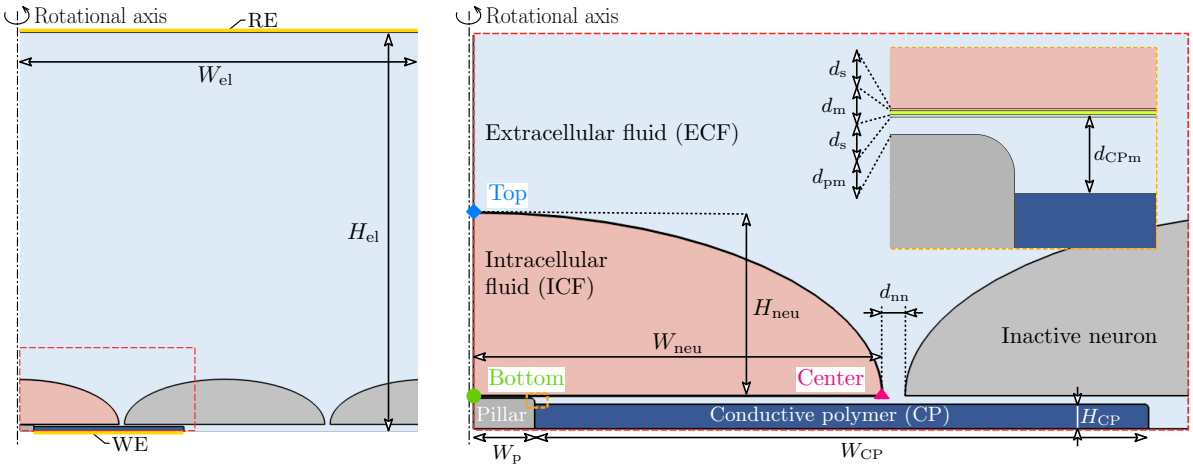



**Figure 3.** (a) Section of the 2D-axisymmetric geometry used in this work. The active neuron is shown in pink and the CP in blue. Domains in grey are considered inactive and are not included in the simulation space. Metal contacts (WE and RE) with applied potentials are shown by thick yellow lines. (b) Zoom of the active neuron domain, highlighting some relevant points at the neuron membrane: "Top" (blue), "Center" (red), and "Bottom" (green) that will be employed in the figures in the Results section. Orange dashed lines (inset) report an additional zoom of the CP-Neuronal cleft. Additional description of the geometrical parameters and their reference values are reported in Table S5.

### *2.3. Geometry*

The proposed modeling approach allows us to spatio-temporally resolve ionic gradients and potential drops in the continuous space including the double layer charge at the interfaces. As such, this model demands for a refined space discretization capable to reproduce sub-nanometer features. To reduce computational cost we consider a 2D-axisymmetric geometrical domain that cuts down the model complexity to the one of a 2D model but restricts geometry to axial symmetry [59]. The reference simulation structure used in this work is shown in Fig. 3.a. It includes an active neuron cell (light red) shaped as a halved oblate ellipsoid (dome) laying on a ring-shaped ionic actuator (dark blue) immersed in an electrolyte bath (light blue). Lateral neurons (grey, on the right) are non-active and are included by means of encumbrance to resemble realistic neighboring cells in a cultured setting. Obviously, their dome shape cannot be enforced in the 2D-axisymmetrical model so they are essentially rings limiting the ion transport in the vertical direction as in a realistic culture. An oxide pillar (grey, on the bottom left) is included to keep the neuron at a given distance from the polymer, leaving an electrolyte cleft between the two. A zoom-in view of the active neuron boundaries is reported in Fig. 3.b. If not otherwise specified, we use the values in Table S5 for the geometrical parameters.

## 3. Results

### *3.1. Ideally-selective CP (isCP)*

Figure 4 shows the working principle of ion actuation in the isCP case study. Initially, the ionic actuator is biased at a negative potential (dedoped state), $V_{\text{app}} = -1$ V, which corresponds to a very small hole concentration, $p$, in the CP so that the $PSS^-$ charges are mostly compensated by the stored $K^+$ ions. By ramping the applied potential, holes are injected into the film (or, in other words, electrons are transferred from the PEDOT into the metal contact) and potassium ions are released in the ECF producing a constant ionic current in accordance with the volumetric capacitive behavior of the CP. The cations diffuse towards the neuron and increase the local extracellular concentration, $[K^+]$, in the proximity of the cell membrane resulting in membrane depolarization. As shown in Fig. 4.a, a $V_{\text{app,max}} = -0.65$ V produces $\Delta[K^+] = 20$ mM and is able to induce an *ionic* AP. By increasing the maximum value of the applied voltage, one can further increase the released dose of $K^+$ and hence the local $[K^+]$, thereby eliciting multiple APs. An example is shown in Fig. 4.b, where $V_{\text{app,max}} = -0.5$ V induces two consecutive ionic APs. The ionic flux emitted by the CP during the release is proportional to the slope of the ramp stimulus $V_{\text{app}}(t)$, namely $v = dV_{\text{app}}(t)/dt$. Therefore, higher $v$ yields larger transient perturbations of the local concentration of $K^+$. This is shown in Fig. 4.c, where the neuron reaches a configuration of depolarization block [60] due to the large perturbation of $[K^+]$. One should note that, since the CP is assumed perfectly selective to $K^+$ ions ($\gamma_{Na^+} = 0$), the increase of $[K^+]$ induced by the ionic actuator produces a decrease of $[Na^+]$ and an increase of $[Cl^-]$ (not shown), owing to electroneutrality. While changes in sodium concentration also contribute to membrane depolarization, their effect is quite limited compared to potassium. This is highlighted in Fig. S1, where we show the reversal potentials as a function of the changes in the extracellular ion concentration. We remark that the initial value of the applied potential $V_{\text{app}} = -1$ V to keep the polymer in a dedoped state depends on the choice of the CP (PEDOT-PSS), the metal contact, and the reference electrode. Therefore, it may vary with different instances of model parameters. Given the purely capacitive nature of CPs assumed in this work, and since we do not model redox reactions between the polymer and the extracellular fluid, no current flows from the WE to RE under constant applied potential.

We point out that, during $K^+$ release, the bottom side of the neuron is hyperpolarized, while the upper one is depolarized (see the last row in Fig. 4); and the extent of such perturbations is enhanced by larger $v$. This is due to the drift component of the ionic flux released by the CP, which acts as anodal source of electrical stimulation [61]. Incidentally, this may raise the question that the electrical component may be the main neuromodulation drive of the firing patterns observed in Fig. 4. To rule out this hypothesis, we repeated the same simulations while keeping the reversal potentials fixed to their baseline values (see Fig. S2). Since no APs are elicited in this case, we can confirm that the ionic neuromodulation, and thus the release of potassium ions, is responsible for the neural activity observed in Fig. 4. Fig. S2 also suggests

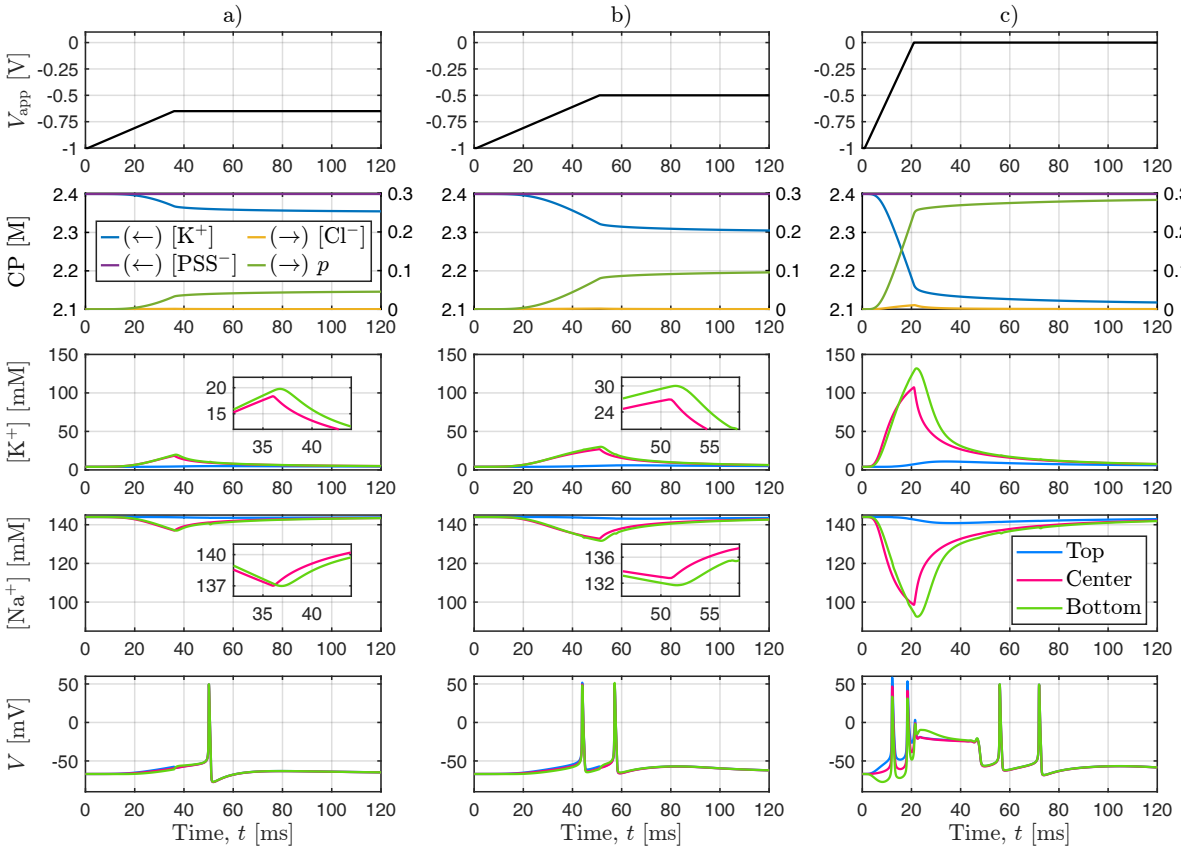



**Figure 4.** Ideally-selective CP (isCP): examples of ionic neuromodulation transients. Different profiles for the applied potential to the CP are considered: a) $V_{\mathrm{app,max}} = -0.65$ V, $v = 10$ V/s, b) $V_{\mathrm{app,max}} = -0.5$ V, $v = 10$ V/s, c) $V_{\mathrm{app,max}} = 0$ V, $v = 50$ V/s. The rows show, in order: 1) the potential applied to the metal contact below the CP, 2) the concentrations of ions and holes inside the CP, the extracellular concentrations for 3) $K^+$ and 4) $Na^+$, and 5) the membrane potential. The labels "top", "center" and "bottom" refer to the points marked in Fig. 3.b. In the second row, two different scales are adopted for $[K^+]$, $[PSS^-]$ and $[Cl^-]$, $p$, respectively (see arrows in the legend).

that the slope of the actuation potential must be small enough to limit the electric field generated by the ionic actuator and therefore ensure a ionic-only stimulation. We point out that, owing to the capacitive nature of the CP, the currents delivered through ramp profiles of $V_{\mathrm{app}}(t)$ resemble pulse-shaped waveforms typically used in neuroengineering devices for electrical stimulation [62], [63].

Figure 5 reports different snapshots of the 2D-axisymmetric spatial distributions of ionic concentrations and potentials of the transient in Fig. 4.a. Three time points are considered: (left) at the end of $K^+$ release ($t = 35$ ms), (middle) at the peak of the elicited AP ($t = 46.87$ ms), and (right) during the post-AP re-equilibration of ions in the ECF ($t = 80$ ms). A close inspection of the extracellular potential (fourth row) confirms a non-negligible electrical gradient during release (e.g., the total potential drop in the neuron-CP cleft is a few mV at $t = 35$ ms), which is responsible for the aforementioned electric component of neurostimulation.

The ion-release performance of the ionic actuator depends on both CP properties

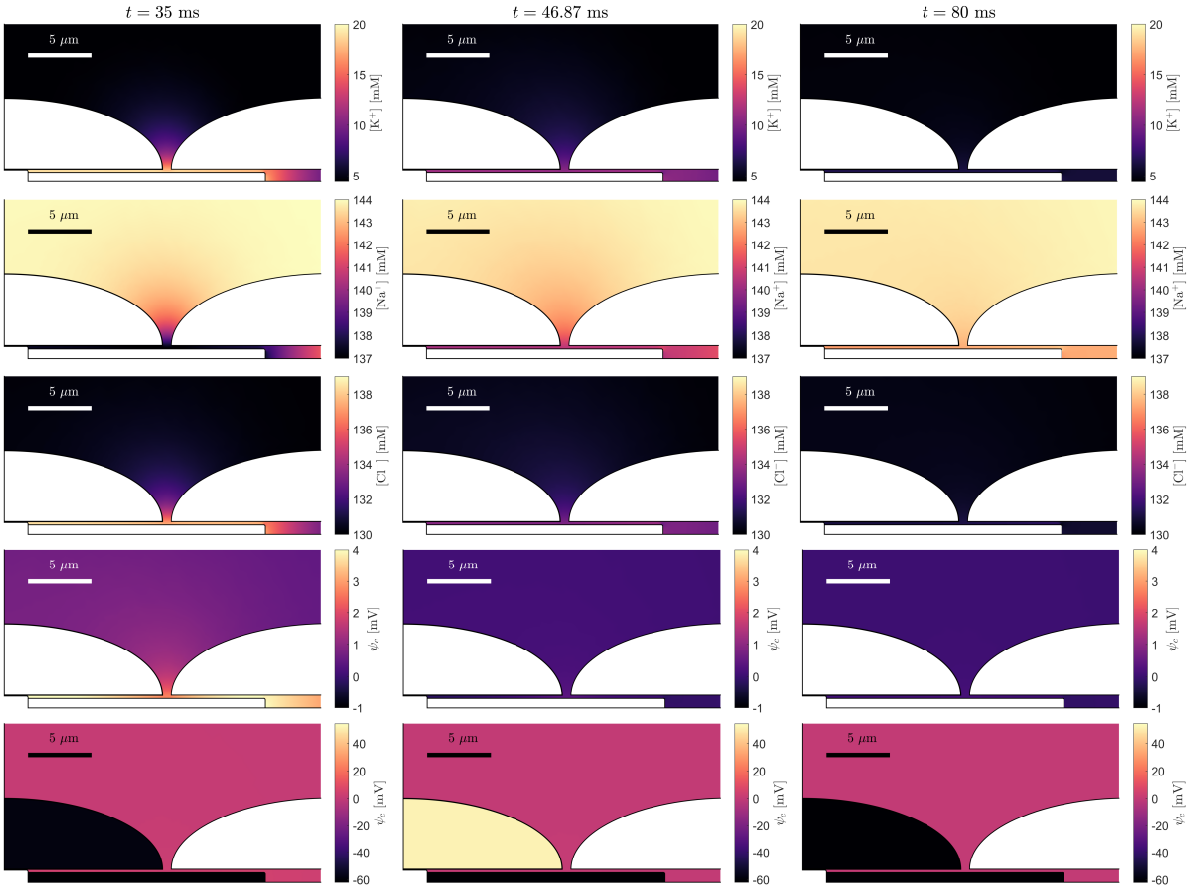



**Figure 5.** Ideally-selective CP (isCP): 2D-axisymmetric cutplanes illustrating the spatial distributions of different physical variables taken during the transient simulation in Fig. 4.a. Three time snapshots are considered: (left) at the end of $K^+$ release ($t$ = 35 ms), (middle) at the peak of the AP ($t$ = 46.87 ms), and (right) during the post-AP re-equilibration of ions in the ECF ($t$ = 80 ms). The rows show, in order: the extracellular concentrations of 1) $K^+$, 2) $Na^+$, and 3) $Cl^-$, the electric potential 4) in the ECF only and 5) in both the ICF and ECF. Note the different color scale in rows 4) and 5).

and geometrical factors. In fact, on one side the available ionic dose is strictly related to the number of fixed charges incorporated in the film. For example, Fig. S3 shows that the maximum releasable dose of $K^+$ decreases with decreasing [$PSS^-$] in the CP. Once the CP is depleted from cations, $Cl^-$ anions start entering the CP to balance the excess holes injected by the metal contact. On the other side, the encumbered space around CP helps to maintain the perturbation of [$K^+$] in the bottom part of the neuron for longer times, thus facilitating ionic APs. This is shown in Fig. S4 where, for the same $V_{app}$ profile, the change in extracellular [$K^+$] decreases for larger gaps between the active and lateral neurons (i.e., low surface density of neurons). A similar effect is obtained for larger clefts between the neuron and the CP, as illustrated in Fig. S5.

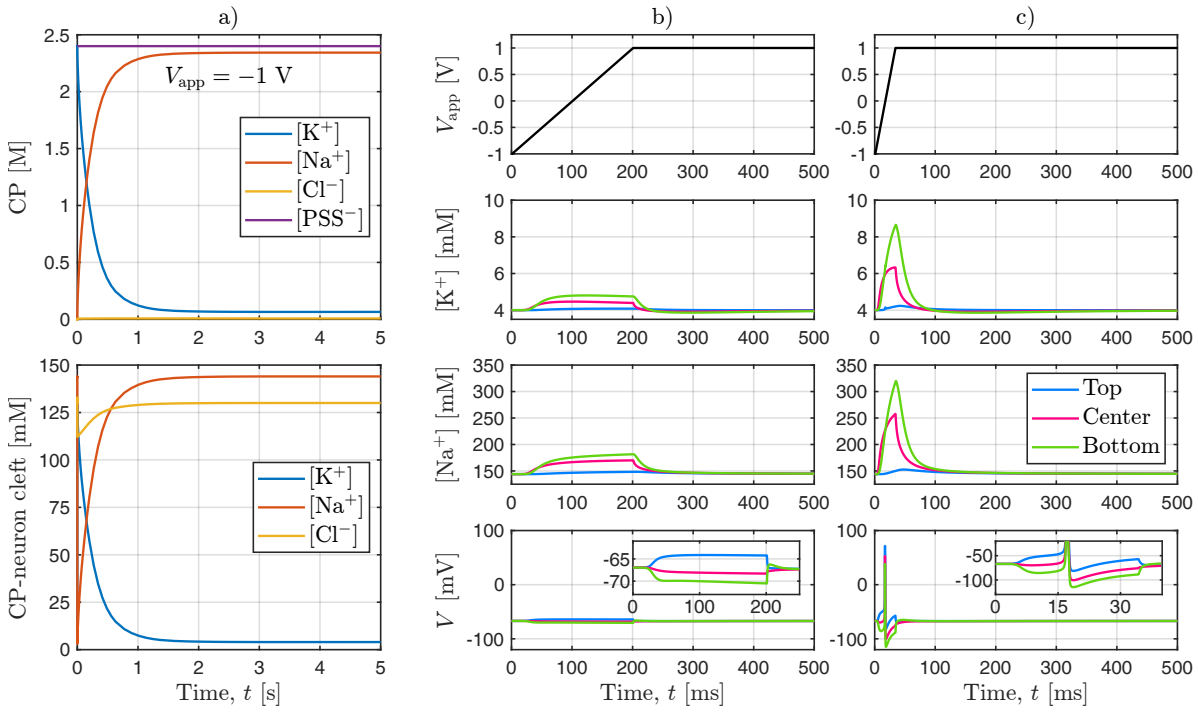



**Figure 6.** Non-selective CP (nsCP). a) Ion-retention study of the $K^+$-preconditioned CP immersed into a physiological fluid while biased at $V_{app} = -1$ V. The top figure shows the time-evolution of the ion concentrations inside the CP, while in the bottom the ones in the CP-neuron cleft. b-c) Examples of ionic neuromodulation transients performed immediately after the ion-retention study. Different slopes for the applied potential are considered (with $V_{app,max} = 1$ V): a) $v = 10$ V/s and b) $v = 60$ V/s. The rows show, in order: 1) the potential applied to the CP, the extracellular concentrations for 2) $K^+$ and 3) $Na^+$, and 4) the membrane potential.

### *3.2. Non-selective CP (nsCP)*

Figure 6 illustrates the working principle of ion actuation in the nsCP case study. Since no selectivity to $K^+$ is enforced, we first tested the CP capability of maintaining a pre-charged dose of $K^+$ ions, i.e., we assume that the polymer has been initially preconditioned with pure KCl that is then replaced with the extracellular fluid. In Fig. 6.a we report the simulation results of such ion-retention study, starting from a CP pre-charged with $K^+$ and held in the undoped state ($V_{app} = -1$ V). Being permeable also to $Na^+$, the CP rapidly evolves to a configuration of thermodynamic equilibrium where $K^+$ and $Na^+$ concentrations retain the same ratio as in the ECF, corresponding to $[K^+]_{CP} = 65.1$ mM, $[Na^+]_{CP} = 2.34$ M, and so $[K^+]_{CP}/[Na^+]_{CP} = 2.8\%$. Therefore, the CP fails to maintain most of the pre-charged $K^+$ dose, which is released in the ECF in an uncontrolled fashion. Compared to the isCP, the available potassium in the nsCP case is hence reduced by a remarkable factor (37 in our case).

Starting from the condition resulting from the transient in Fig. 6.a, we simulate two examples of ionic actuation with applied stimulus featuring either $v = 10$ V/s or $v = 60$ V/s (Fig. 6.b and c, respectively). Differently to the isCP case, the injection of holes induces a release of both $K^+$ and $Na^+$ ions. Since $Na^+$ is the dominant ion in the CP,

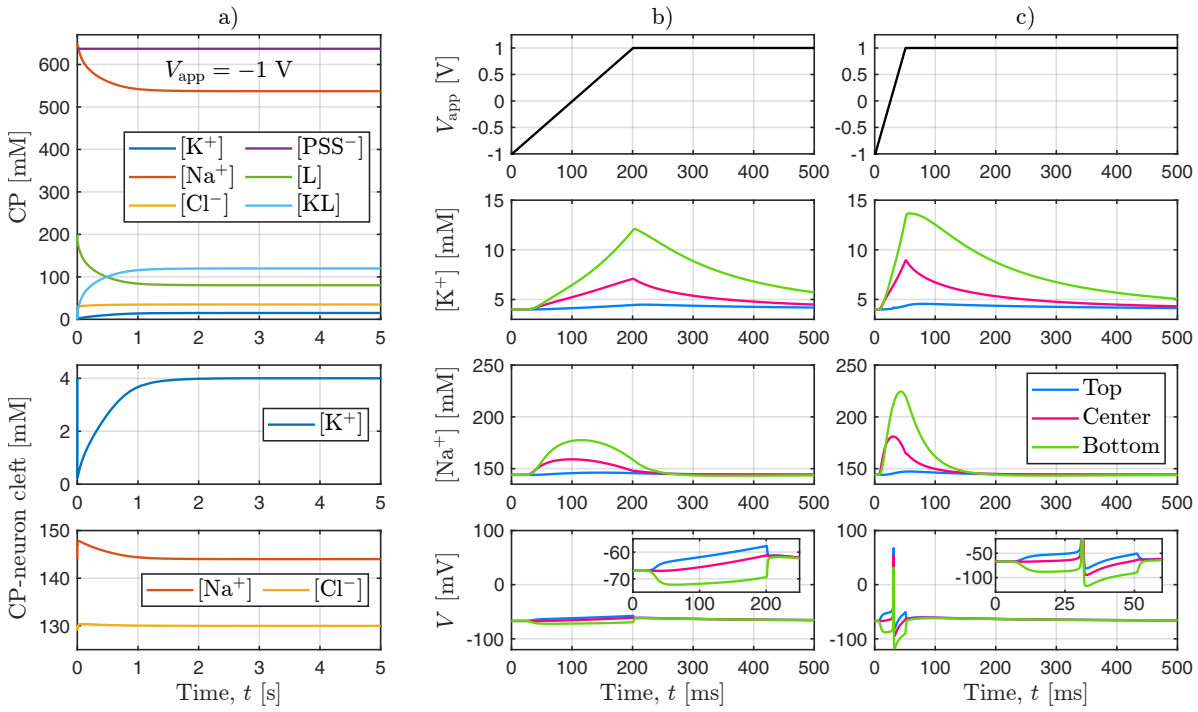



**Figure 7.** Ionophores-induced selective CP (ionoCP). a) Re-equilibration study with CP biased at $V_{app} = -1$ V to allow the formation of KL complexes. The first row shows the ion concentrations inside the CP, while the second and third rows the ones in the cleft between the neuron and the CP. b-c) Examples of ionic neuromodulation transients after the re-equilibration study. Different slopes for the applied potential are considered (with $V_{app,max} = 1$ V): b) $v = 10$ V/s and c) $v = 40$ V/s. The rows show, in order: 1) the potential applied to the CP, the extracellular concentrations for 2) $K^+$ and 3) $Na^+$, and 4) the membrane potential.

the ion release predominantly affects the local concentration of sodium ions in the ECF. In contrast to what we observed in Fig. 4 for the isCP, $[K^+]$ here increases locally by only a few mM, despite having applied a larger stimulus, $V_{app,max} = 1$ V versus -0.65/-0.5 V in Fig. 4. Another important finding is that the membrane potential induced by the nsCP is mostly due to the electric field produced by the applied potential rather than by the perturbation of the ionic concentrations (mostly $[Na^+]$). As shown in Fig. 6.c, an AP can eventually be elicited if $v$ is increased to, e.g., $v = 60$ V/s. However, the AP persists with an almost identical time course even when the reversal potentials of the neuron are kept fixed to their baseline values (see Fig. S6). We will thereafter refer to this kind of stimulation of action potentials as *electric*, i.e., APs not directly induced by the perturbation of the extracellular ionic concentrations.

### *3.3. Ionophores-induced selective CP (ionoCP)*

We chose the ionoCP properties according to optimality criteria based on simulations employing a reduced model of the CP/ECF interaction (see Supplementary Note 3). The optimization parameters were the equilibrium constant of ionophores $\beta_{KL}$ and the concentration of fixed charges in the polymer $[PSS^-]$. The backward rate constant was

set based on the literature ($k_{KL,b}$ = $10^{-4}$ 1/s as in [64]), while the forward one is by definition $k_{KL,f} = k_{KL,b} \cdot \beta_{KL}$. The optimum was evaluated adopting as figure of merit the $[K^+]$ change achieved in the finite-volume ECF at steady state (representative of the ionic stimulation achievable by the ionoCP), for a given applied $V_{app,max}$. Fig. S7.a-c show $[K^+]$ vs $[PSS^-]$ curves that were obtained for different total concentrations of ionophore in the system, $[L]_{tot}$, and $V_{app,max}$ = 2 V. Interestingly, in all cases, the optimum association constant was $\beta_{KL}$ = 100 $M^{-1}$. Even though larger concentrations of ionophores induce more ionic release, we chose $[L]_{tot}$ = 200 mM corresponding to half of the maximum steric occupancy of a very common $K^+$-ionophore [65]. Therefore, the optimum from Fig. S7.b was used, i.e., $[PSS^-]$= 637 mM. Further analysis regarding the maximum voltage applied at the CP electrode, $V_{app,max}$, revealed that the optimum amount of $[PSS^-]$ depends on this parameter with direct proportionality (Fig. S7.d) but changes on the above-defined figure of merit are modest (Fig. S7.e).

Figure 7 reports the simulation results for ion actuation in the ionoCP case study with the optimized parameters described above. Here, ionophores L are embedded in the CP and provide selectivity to $K^+$ ions by forming $K^+$-L complexes (hereafter, simply KL). The formation process is shown in Fig. 7.a, where a CP pre-charged with $Na^+$ is immersed into the extracellular fluid and held at the dedoped state $V_{app}$ = −1 V while ionophores bind the free $K^+$ ions entering from the ECF. At equilibrium, the ratio between potassium (both free and complexed) and sodium ions in the CP results larger than in the ECF (and thus larger than in the nsCP case seen in Fig. 6). Specifically, we observe $[K^+]_{CP}$ = 14.9 mM, [KL] = 119.8 mM, $[Na^+]_{CP}$ = 537.1 mM, and so $([K^+]_{CP} + [KL])/[Na^+]_{CP}$ = 25.1% (instead of 2.8% as in the nsCP case).

Figure 7.b and c show two examples of ionic actuation with the ionoCP, for $v$ = 10 V/s and $v$ = 40 V/s, respectively ($V_{app,max}$ = 1 V). Because of the selectivity induced by the ionophores and their relatively low association constant, a much higher perturbation of $[K^+]$ is obtained with respect to the non-selective case of Fig. 6. However, the main hallmark of the ionophores' presence is the prolonged release of $K^+$ due to the unbinding of the KL complexes that continues for several hundreds of ms after the end of the $V_{app}$ ramp (compare Fig. 7.b and Fig. 6.b). This is also shown in Fig. S8, where the local $[K^+]$ at the bottom of the neuron is plotted for different $V_{app,max}$ and for different time snapshots after the end of the release, in both the ionoCP and nsCP cases. Fig. 7.c shows that an AP is obtained by increasing $v$ to 40 V/s. Interestingly, a closer analysis revealed that such AP is a mixed ionic/electric AP since it is not elicited if the reversal potentials are kept fixed to their baseline values (see Fig. S9). In other words, the $K^+$-induced depolarization lowers the threshold for electrical stimulation necessary to induce firing.

An important feature of the ionoCP device, is the possibility of operating with a single reservoir (i.e., the ECF) as a recyclable source of ions. Figure 8 shows a preliminary investigation of this possibility. Namely, we considered actuation transients with voltage pulses featuring both rise and fall ramps, possibly with different slopes. The falling ramp allows the CP to return to its dedoped state and thus recharged with

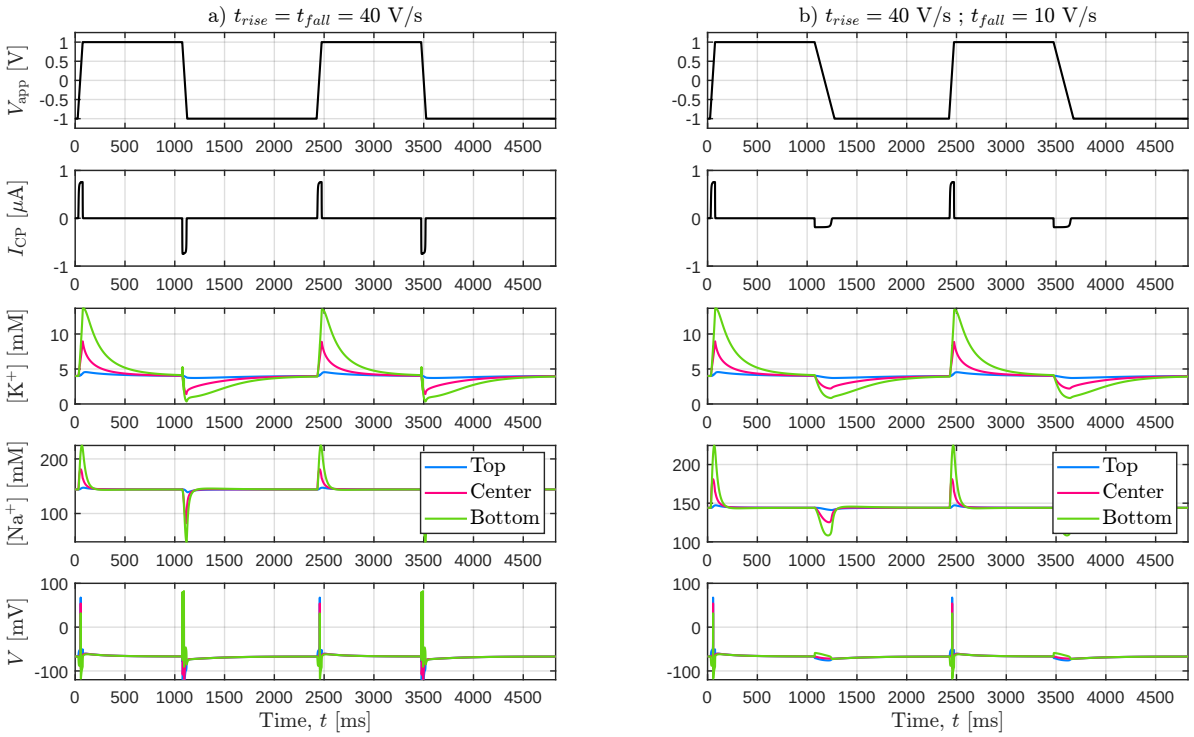



**Figure 8.** Test of the reversibility of the operation of the ionophores-induced selective CP (ionoCP). Potential pulses with different rise and fall times are applied at the CP during the actuation cycle. From top to bottom, rows indicate: 1) the voltage applied to the CP $V_{\text{app}}$, 2) the current emitted by the CP, $I_{\text{CP}} = F\frac{d}{dt}\left(\int_{\text{CP}} p\, d\Omega\right)$, the extracellular concentration of 3) [K$^+$], and 4) [Na$^+$], and, 5), the membrane potential $V$. In a), fast slopes of 40 V/s are used for both rising and falling edges, causing electrically-induced APs at each front followed by a gradual return to the electrochemical equilibrium. In b), a slower slope of 10 V/s is used on the falling edge (i.e., return to baseline) that does not induce APs. Besides, two consecutive pulses are displayed for both cases, showing no perceptible difference in the second pulse compared to the first one in terms of potential waveform and ionic profiles. An interesting observation is that the ionic emission and recharge dynamics are very different, as they reflect two different mechanisms: the first one is the ionic release limited by K$^+$ diffusion to the bulk of the extracellular fluid, while the second one is the depletion of ions in the proximity of the CP/electrolyte interface, ultimately limited by the diffusion of ions from the bulk to the solution.

ions diffusing from the ECF. We extended the simulation time to include many pulses, thereby showing that a full recovery of the baseline equilibrium between CP and ECF is achieved in less than 1 s after the falling ramp. Figure 8 also indicates that the return to baseline of the potential applied to the CP (or, in other words, the CP recharge of ionic carriers) can be seen as an actuation mechanism as well, since the descending voltage ramp can induce both potential and ion concentration perturbations in the electrolyte. The rate of the recovering step will thus determine the extent of the actuation both in terms of modulation of the ionic concentrations and in terms of the transient electric field in the extracellular domain surrounding the neuron.

The analysis above suggests that, despite not being sufficient to handle a fully ionic neuromodulation, the functionalized ionoCP is still able to enhance the excitability of the neuron and to operate in a reversible fashion. The reader should note that ionophores

are here modeled as mobile species in our framework. However, this is not a critical choice since results are very mildly affected by considering such species to be covalently bound to the polymer backbone or with very low diffusion coefficients (see Fig. S10).

### *3.4. Ionophores-induced selective CP (ionoCP): effect on AMPA synapses*

To further test the neuromodulation capabilities of the ionoCP film, we evaluate the response of the neuron undergoing ionic actuation in the presence of an excitatory synaptic event. First, we determined the synaptic conductances $\overline{g}_{\mathrm{K,syn}}$, $\overline{g}_{\mathrm{Na,syn}}$ (see Fig. 2, right) as the minimum values required to elicit APs (see Fig. S11). Thus, we investigated the efficacy of synaptic transmission for different scaling of the synaptic conductances and for increasing extents of ionic release (see Fig. 9). We point out that, since the neural membrane is described by a reduced HH model [43], the $\overline{g}_{\mathrm{X}_i,\mathrm{syn}}$ are regarded as phenomenological terms lumping the postsynaptic conductances of all the AMPA synaptic receptors, rather than the dynamics of a single synapse. In this perspective, variations of $\overline{g}_{\mathrm{X}_i,\mathrm{syn}}$ qualitatively represent changes in the presynaptic drive to the neuron. Figure 9.a shows a synaptic event occurring 30 ms after an ionic actuation transient that fails to induce an AP (0.4 $g_{\mathrm{X}_i,\mathrm{syn}}$, $V_{\mathrm{app,max}}$ = 0 V). Successful synaptic transmission can be achieved through larger presynaptic drive (0.7 $g_{\mathrm{X}_i,\mathrm{syn}}$ in Fig. 9.b) or more ionic release ($V_{\mathrm{app,max}}$ = 1 V) in Fig. 9.c, since the postsynaptic current gets enhanced. Figures 9.A-F illustrate a more extensive study, where elicited APs are mapped in the two-dimensional space of synaptic conductances scaling – extent of ionic release, for different delays between ionic stimulation and the synaptic event. These results clearly suggest that excitatory synaptic transmission is facilitated in the presence of the ionic actuators releasing $K^+$. Moreover, thanks to the slow release granted by ionophores, such facilitation lasts up to hundreds of milliseconds with progressively milder intensity.

## 4. Discussion

### *4.1. Modeling of neuromodulation through ionic actuators*

In this work, we introduced a finite-element model to describe the interaction between a CP-coated microelectrode and a neuron soma. To the extent of our knowledge, this is the first computational framework that solves the coupled equations for the dynamics of an ionic actuator, the cellular fluids, and the neural membrane. We used our simulation framework to investigate the controlled delivery of potassium in the extracellular fluid as a neuromodulation mean. We considered three case studies for the CP, with different levels of selectivity to $K^+$: ideally-selective (isCP), non-selective (nsCP), and ionophores-induced selective (ionoCP).

The isCP case, despite being unrealistic, allowed us to showcase the technological potential of ionic neuromodulation assuming a CP film able to selectively store and release in the ECF only potassium. A local increase of $[K^+]$ allows steering a target

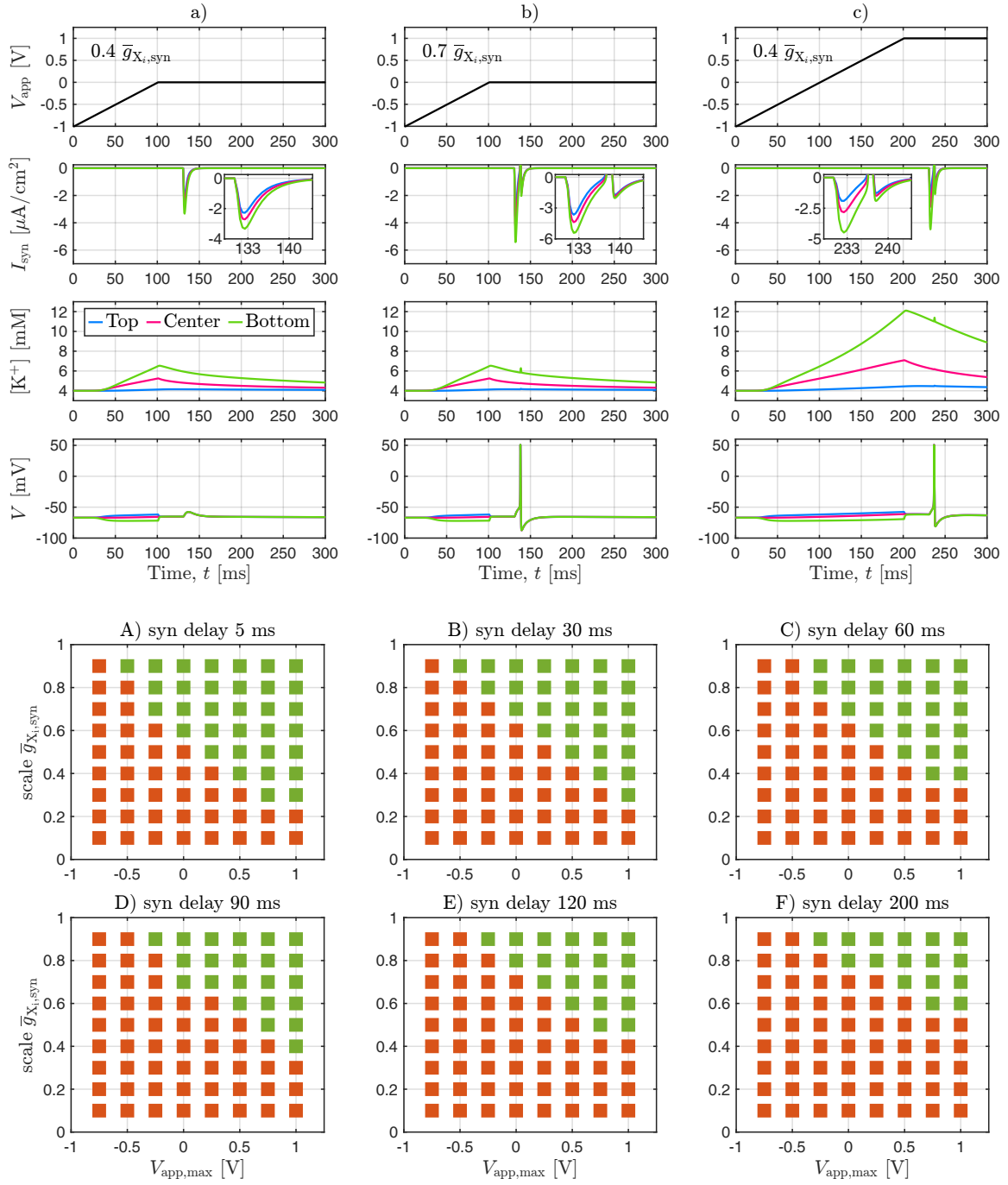



**Figure 9.** Ionophores-induced selective CP (ionoCP) and synaptic transmission. Top) Examples of synaptic events taking place 30 ms after the end of the ionic release. The one in a) fails to induce an AP (0.4 $g_{X_i,syn}$, $V_{app,max}$ = 0 V). Successful synaptic transmission can be achieved by increasing the postsynaptic current with, e.g., b) a larger presynaptic drive (0.7 $\overline{g}_{X_i,syn}$) or c) higher applied potential ($V_{app,max}$ = 1 V). The rows show, in order: 1) the potential applied to the CP, 2) the synaptic current $I_{syn} = I_{K,syn} + I_{Na,syn}$ 3) the extracellular concentrations for $K^+$, and 4) the membrane potential. Bottom) Systematic evaluation of the synaptic transmission's efficacy in the space of $V_{app,max}$ and the scaling of $\overline{g}_{X_i,syn}$. Each subplot corresponds to a different delay between the synaptic event and the end of ionic release. In order, from A to F: 5, 30, 60, 90, 120, and 200 ms. Green squares: AP elicited. Red squares: no AP elicited.

neuron to regimes of firing or depolarization block by affecting its intrinsic excitability. These are well-established facts in literature [66], which can be leveraged to elicit or inhibit neural activity, respectively. We note that, regarding inhibition, depolarization block is a mechanism putatively exploited by neurons to limit the overall network activity also *in-vivo* [67]. A FEM modeling framework enables to link such neuromodulation targets to the physical and geometrical parameters of the CP and its surroundings, as well as the stimulation protocols. Examples of such capabilities have been showcased by changing the potential waveform applied to the CP, the maximum releasable dose of potassium, the lateral encumbrance due to other cells, and the size of the CP-neuron cleft. Notwithstanding, similar analyses can be performed for all the other model parameters, e.g., the CP size, the material of the metal contact, or other intrinsic parameters of the CP, such as the volumetric capacitance, in support of thoughtful engineering choices.

At the opposite side of the selectivity spectrum, the nsCP case illustrates how a bare PEDOT:PSS-coated electrode is not effective as ionic neuromodulator. Indeed, it is not able to hold a pre-charged potassium dose, e.g., coming from a preconditioning stage in a different electrolyte. Further, it mainly conveys electric stimuli to target neurons. This is an important sanity check for our simulation deck, since such coatings are routinely used in electric neurostimulation devices to enhance properties such as contact impedance, charge storage capacitance, and biocompatibility [68], [69], and our model confirms that such electrodes can elicit APs through electrical stimulation but not via ionic perturbation.

The ionoCP case is investigated as a possible ionic neuromodulation device endowed with ionophores that confer selectivity. Indeed, the possibility to embed ionophores in the polymeric backbones has already been proven in the literature [21]–[23], even though they were employed for ion-sensing devices rather than for ion delivery. A second important challenge addressed by our solution is the operation in a single reservoir, i.e., the ECF, which holds the promise to act as a recyclable source of ions to perform unlimited stimulation, reconciling miniaturization without handling multiple reservoirs as in other iontronic solutions [13], [70]. Our findings suggest that ionophores with an equilibrium constant around $\beta_{\mathrm{KL}} = 100\ \mathrm{M}^{-1}$ give the best trade-off between selectivity and release performance. This value is smaller than those used in sensor applications (e.g., $\beta_{\mathrm{KL}} = 1026.2 \pm 118.3\ \mathrm{M}^{-1}$ in [21]) as too strong complexes are difficult to dissociate during the actuation phase. Notwithstanding, our framework can be utilized to test realistic ionophore species [71], [72], by instantiating the respective parameters. With the optimized ionoCP, we have shown *in-silico* that, despite its performances being highly inferior with respect to the isCP, it is still possible to induce a significant local perturbation of $[\mathrm{K}^+]$ up to tens of mM above the extracellular bulk concentration, sufficient to enhance the sensitivity of the neuron to other stimulation means (e.g., electrical stimulation), as well as to facilitate excitatory synaptic transmission. A similar neuromodulation capability was recently proven *ex-vivo* in retina tissue by microfluid delivery of Ames' medium containing 22 mM $\mathrm{K}^+$ on perforated microelectrode arrays

[73]. This suggests that induced synaptic facilitation provided by ionic neuromodulation may also represent a mean to trigger synaptic plasticity in networks of neurons.

The above analysis led us to conclude that it is difficult to elicit APs by releasing potassium ions only, unless an ideally selective polymer is available. In case the polymer is not selective or only partially selective, APs are essentially elicited by electrical stimulation if the electrode potential is ramped fast, but this cannot be referred to as *ionic actuation*. Further, ideal selectivity for actuation purposes is very hard to achieve with ionophores. The inclusion of synaptic dynamics showed that effects on neural activity driven by ionic actuation are more pronounced through the synaptic pathway rather than those affecting the intrinsic excitability of the neuron. These analyses, despite being qualitative, prompt the need for a description of neuronal dynamics down to the level of synaptic transmission to correctly predict the effects of ionic actuation. Since synaptic dynamics is intrinsically a network phenomenon, more effort must be made to increase the complexity of the simulation deck, while ensuring a viable computational cost. We remark that our conclusions, despite being obtained *in-silico*, are build upon models that have been extensively validated against experiments. Indeed, the two-phase model for the CP has been shown to effectively fit electrochemical data [28]. Moreover, the HH model [43], coupled with lumped dynamics of ions in the cellular fluid, was able to qualitatively capture the firing patterns of interneurons of the rat CA1 hippocampus in seizure-like and spreading depression-like events [50], [51].

### *4.2. Simulation platform*

Our approach based on COMSOL Multiphysics enables seamless integration with other stimulation or sensing devices that may be relevant in neuromodulation applications, like multielectrode arrays (MEAs) [74]. Moreover, the use of a commercial platform has been motivated by its widespread adoption in the computational communities of neuroengineering [33], [34] and electrochemistry [28]–[32], and by its capabilities in bridging the gaps between these two disciplines: the former being very knowledgeable in terms of modeling neural activity and excitation but relying on an ohmic description of the neural milieu, while the latter focusing on the electrodiffusive description of cellular fluids but without taking into account the effects on neuronal activity. We point out that this is an alternative approach compared to that of the computational neuroscience community dealing with drift-diffusion phenomena in the neural microenvironment [39], [75]–[78], which typically embraces open-source software.

### *4.3. Model limitations and outlook*

In this work, we resorted to the PNP model to describe ion electrodiffusion in the cellular fluids. Modeling neural activity with such a level of detail is very computationally demanding and therefore difficult to scale to large spatial domains and more complex geometries. The main reason resides in the building up of electrical double layers at charged interfaces that require very fine spatial meshes with subnanometer resolution.

Therefore, studies in the literature employing this formalism have been hitherto limited to simple neural morphologies such as axons [39]. Alternatively, other studies have focused on neural microdomains [41], [42] with small spatial extension, like nodes of Ranvier [40], spines [79], ion channels [80], and synapses [81]. As an example of the aforementioned computational burden, we observed an average simulation time of about 26 minutes for the studies reported in Fig. 9.B (89 transients lasting 300 ms), while about 33 minutes for those in Fig. 9.D (89 transients lasting 400 ms). Simulations were run in parallel on two servers: the first with an Intel® Xeon® X5690 CPU and 189 GB of RAM while the second with an Intel® Xeon® Gold 6136 CPU and 500 GB of RAM. Further details are reported in Supplementary Note 1. It is thus clear that a reduction in the computational burden is pivotal to pave the way to more realistic descriptions of the *in-vivo* neural milieu, e.g., accounting for detailed neuron morphologies [82] and network interactions [83]. This, in turn, holds the promise to make the presented framework more informative for the design and optimization of ionic actuators, and allows it to handle more complex and realistic cases needed for proper validation against experimental data.

Aiming in this direction, the Kirchhoff-Nernst-Planck (KNP) framework has been developed [58], [75]–[78], [84]. It sensibly reduces the computational burden by enforcing electroneutrality in the resolved space domain and splitting displacement currents among ionic fluxes at the cell membranes. However, the validity of KNP has been assessed for biological electrogenic sources [85] but not during the operation of ionic actuators. Indeed, to date, computation efforts focusing on the sole ionic actuator rely on the PNP [29]–[32]. Before deploying the KNP in our setting, its domain of validity must be determined taking into account the tiny clefts and non-physiological ionic concentrations that may stem from the neuron-CP interaction. A preliminary analysis is shown in Fig. S12, where we report the charge density in the cleft between the CP and the neuron under the ion release by the ionoCP (Fig. S12.a) or the nsCP (Fig. S12.b). Further, we consider the charge in the cleft during a synaptically-induced AP (Fig. S12.c), as an example of physiological electrogenic source. Except for the starting and ending phases of the applied stimulus ramp, at each time point the charge in (b) is similar to that in (c). On the other hand, the charge results more than ten times greater in (a) than in (c). This deviation from electroneutrality persists for the entire duration of ionic release in (a) (hundreds of ms) instead of a single AP's duration in (c) (a few ms). These results suggest that the electroneutrality assumption embraced by the KNP might not hold under the operation of ionic actuators like the ionoCP. A thorough comparison of the PNP model used in this work with a KNP-based model is not in the scope of this work and is left for future investigation.

It is important to remark that in our approach the dynamics of the cellular fluids and the ionic actuator are solved self-consistently. This modeling scheme is rarely pursued, even in established computational frameworks supporting the design of neural interfaces, e.g. for electrical stimulation [86], [87]. Rather, scientists resort to *hybrid models*: first, the extracellular potential is computed with either analytical approximations [37] or finite-element methods (FEM) [38]; second, the response of nerve cells is assessed by

feeding the results of the previous step as input. Similar schemes have been developed also for electrodiffusive models of the neuron-ECF interaction [75]. Assessing the validity of these schemes in the ionic neuromodulation setting may provide further means to reduce the computational cost, thanks to the decoupling of simulations in two problems easier than the original one. To this aim, our model may be instrumental in validating such simplifications. Another advantage of hybrid approaches is to deploy the full potential of simulators of realistic multicompartment models of nerve cells, like NEURON [88], accounting for complex morphological and dynamical features. Unfortunately, our self-consistent framework in COMSOL does not allow us to delegate the solution of the neural membrane dynamics to third-party software. This limits the integration and reusability of models of neural cells previously published in literature [89].

The electrodiffusive formalism employed in this work, as well as the KNP mentioned above, are intrinsically more accurate than the ohmic formalism, where the cellular fluids are considered volume conductors and diffusion mechanisms are neglected. Given its simplicity and low computational cost, the ohmic formalism is widely used to model the interface between neurons and implanted electrodes, both for stimulation [34] and recording [90] studies. However, the lack of a proper description of the ionic transport limits the validity to cases where the electric field is the main vehicle of action potential recording/generation. In Supplementary Note 2 (Sec. "Limit case: ohmic approximation for cellular fluids") we introduce the main equations of the ohmic formalism and show that, in fact, its predictions agree with our model only in limit cases where the cleft between the CP and the neuron is sufficiently large such that the modulations of the ionic concentrations are relatively small. In this comparison, we employed the nsCP since, among our case studies, is the one that best reproduces electrodes routinely used in scenarios of electrical neural stimulation/recording (see Sec. 4.1).

We built our modeling framework with the aim of having the essential features to serve as a benchmark for testing the neuromodulation capabilities of the ionic actuator. The selected features resulted from a compromise between the computational burden of simulations and the spatio-temporal scales of interest, namely those of a single neuron soma discharging up to a few APs, thereby leading to several simplifications. On the neural milieu's side, we modeled the dynamics of $K^+$, $Na^+$, and $Cl^-$ ions, along with the ion channels responsible for the sole generation of action potentials. However, many other ions [1], like $Ca^{2+}$ or $Mg^{2+}$, and ionic channels [36] affects the neural functioning. Furthermore, we neglected homeostatic mechanisms occurring at neural membranes or glial cells that are pivotal for the regulation of the ionic composition in the neural microenvironment [2] and are expected to counteract the operation of ionic actuators. Nevertheless, the effects of such mechanisms manifest at temporal scales longer than the ones of interest in this work. A possible way to capitalize on the aforementioned efforts to reduce the computational burden would be the inclusion of such mechanisms and gain insight into the effects of ionic actuation at longer temporal scales. Similar

considerations apply also to the CP's side, where many non-idealities and parasitic phenomena were neglected. For instance: faradaic conduction in the CP [91], the formation of competing bindings of ionophores with, e.g., $Na^+$ ions [21], series impedance of the electrodes [59], as well as red-ox reaction between the CP and the cellular fluids [55]. Other model simplifications are the usage of uniform and time-invariant parameter values inside domains, in contrast with time variability and reduced ionic diffusivity due to tortuosity effects in the ECF [92], as well as variability in the density of ion channels in different portions of the membrane [93]. Notwithstanding, our multiphysics framework is amenable for the integration of these features to explore their effects on the device performance.

## 5. Conclusion

This work combines the multiphysical description of the most essential set of electrochemical and biological processes regarding neurons under ionic and electrical stimulation in a single comprehensive simulation deck. By including accurate models of ion-transport and transmembrane fluxes we demonstrated *in-silico* that the proposed modeling approach can be a powerful tool to predict neuron excitability and to benchmark the performance of novel neuromodulation devices. As an example of application, we simulated the action of an ionic actuator based on organic mixed ionic-electronic conductors (OMIECs) embedding ionophores and demonstrated its capability to provide single-neuron synaptic facilitation. These efforts are oriented toward versatile integration with iontronic devices aiming at closing the loop of already existing methodologies for neural recording and computation *in-liquido* [94].

## Acknowledgments

This work was supported by the European Union's Horizon 2020 Research and Innovation Programme (IN-FET Project) via the Consorzio Nazionale Interuniversitario per la Nanoelettronica (IU. NET) Consortium under Grant Agreement 862882.

## References

[1] R. Rasmussen, J. O'Donnell, F. Ding, and M. Nedergaard, "Interstitial ions: A key regulator of state-dependent neural activity?" *Progress in Neurobiology*, vol. 193, 2020. DOI: 10.1016/j.pneurobio.2020.101802.

[2] G. G. Somjen, *Ions in the Brain: Normal Function, Seizures, and Stroke*. Oxford University Press, 2004, ISBN: 9780195151718.

[3] B. Frankenhaeuser and A. L. Hodgkin, "The after-effects of impulses in the giant nerve fibres of Loligo.," *The Journal of physiology*, vol. 131, no. 2, 1956. DOI: 10.1113/jphysiol.1956.sp005467.

[4] M. Balestrino, P. G. Aitken, and G. G. Somjen, "The effects of moderate changes of extracellular K+ and Ca2+ on synaptic and neural function in the CA1 region of the hippocampal slice," *Brain Research*, vol. 377, no. 2, 1986. DOI: 10.1016/0006-8993(86)90863-2.

[5] P. Y. Shih, L. P. Savtchenko, N. Kamasawa, *et al.*, "Retrograde Synaptic Signaling Mediated by K+ Efflux through Postsynaptic NMDA Receptors," *Cell Reports*, vol. 5, no. 4, 2013. DOI: 10.1016/j.celrep.2013.10.026.

[6] L. M. Grover and T. J. Teyler, "Effects of extracellular potassium concentration and postsynaptic membrane potential on calcium-induced potentiation in area CA1 of rat hippocampus," *Brain Research*, vol. 506, no. 1, 1990. DOI: 10.1016/0006-8993(90)91198-P.

[7] D. M. Durand, E. H. Park, and A. L. Jensen, "Potassium diffusive coupling in neural networks," *Philosophical Transactions of the Royal Society B: Biological Sciences*, vol. 365, no. 1551, 2010. DOI: 10.1098/rstb.2010.0050.

[8] J. V. Raimondo, R. J. Burman, A. A. Katz, and C. J. Akerman, "Ion dynamics during seizures," *Frontiers in Cellular Neuroscience*, vol. 9, no. OCT, 2015. DOI: 10.3389/fncel.2015.00419.

[9] S. F. Traynelis and R. Dingledine, "Potassium-induced spontaneous electrographic seizures in the rat hippocampal slice," *Journal of Neurophysiology*, vol. 59, no. 1, 1988. DOI: 10.1152/jn.1988.59.1.259.

[10] D. Pietrobon and M. A. Moskowitz, "Chaos and commotion in the wake of cortical spreading depression and spreading depolarizations," *Nature Reviews Neuroscience*, vol. 15, no. 6, 2014. DOI: 10.1038/nrn3770.

[11] A. J. Hansen and T. Zeuthen, "Extracellular ion concentrations during spreading depression and ischemia in the rat brain cortex," *Acta Physiologica Scandinavica*, vol. 113, no. 4, 1981. DOI: 10.1111/j.1748-1716.1981.tb06920.x.

[12] G. Ullah and S. J. Schiff, "Tracking and control of neuronal Hodgkin-Huxley dynamics," *Physical Review E - Statistical, Nonlinear, and Soft Matter Physics*, vol. 79, no. 4, 2009. DOI: 10.1103/PhysRevE.79.040901.

[13] J. Isaksson, P. Kjäll, D. Nilsson, N. Robinson, M. Berggren, and A. Richter-Dahlfors, "Electronic control of Ca2+ signalling in neuronal cells using an organic electronic ion pump," *Nature Materials*, vol. 6, no. 9, 2007. DOI: 10.1038/nmat1963.

[14] I. Uguz, C. M. Proctor, V. F. Curto, *et al.*, "A Microfluidic Ion Pump for In Vivo Drug Delivery," *Advanced Materials*, vol. 29, no. 27, 2017. DOI: 10.1002/adma.201701217.

[15] C. M. Proctor, I. Uguz, A. Slezia, *et al.*, "An Electrocorticography Device with an Integrated Microfluidic Ion Pump for Simultaneous Neural Recording and Electrophoretic Drug Delivery In Vivo," *Advanced Biosystems*, vol. 3, no. 2, 2019. DOI: 10.1002/adbi.201800270.

[16] M. Berggren, E. D. Głowacki, D. T. Simon, E. Stavrinidou, and K. Tybrandt, "In Vivo Organic Bioelectronics for Neuromodulation," *Chemical Reviews*, vol. 122, no. 4, pp. 4826–4846, 2022. DOI: 10.1021/acs.chemrev.1c00390.

[17] B. D. Paulsen, K. Tybrandt, E. Stavrinidou, and J. Rivnay, "Organic mixed ionic–electronic conductors," *Nature Materials*, vol. 19, no. 1, 2020. DOI: 10.1038/s41563-019-0435-z.

[18] Z. J. Du, G. Q. Bi, and X. T. Cui, "Electrically Controlled Neurochemical Release from Dual-Layer Conducting Polymer Films for Precise Modulation of Neural Network Activity in Rat Barrel Cortex," *Advanced Functional Materials*, vol. 28, no. 12, 2018. DOI: 10.1002/adfm.201703988.

[19] K. M. Woeppel, X. S. Zheng, Z. M. Schulte, N. L. Rosi, and X. T. Cui, "Nanoparticle Doped PEDOT for Enhanced Electrode Coatings and Drug Delivery," *Advanced Healthcare Materials*, vol. 8, no. 21, 2019. DOI: 10.1002/adhm.201900622.

[20] C. Tan, N. Kushwah, and X. T. Cui, "Electrically controlled neurochemical delivery from microelectrodes for focal and transient modulation of cellular behavior," *Biosensors*, vol. 11, no. 9, 2021. DOI: 10.3390/bios11090348.

[21] A. Villarroel Marquez, G. Salinas, M. Abarkan, *et al.*, "Design of Potassium-Selective Mixed Ion/Electron Conducting Polymers," *Macromolecular Rapid Communications*, vol. 41, no. 12, 2020. DOI: 10.1002/marc.202000134.

[22] S. Wustoni, C. Combe, D. Ohayon, M. H. Akhtar, I. McCulloch, and S. Inal, "Membrane-Free Detection of Metal Cations with an Organic Electrochemical Transistor," *Advanced Functional Materials*, vol. 29, no. 44, 2019. DOI: 10.1002/adfm.201904403.

[23] M. Jeszke, K. Trzciński, J. Karczewski, and E. Luboch, "Investigation of poly(3,4-ethylenedioxythiophene) deposition method influence on properties of ion-selective electrodes based on bis(benzo-15-crown-5) derivatives," *Electrochimica Acta*, vol. 246, 2017. DOI: 10.1016/j.electacta.2017.05.197.

[24] M. Sessolo, J. Rivnay, E. Bandiello, G. G. Malliaras, and H. J. Bolink, "Ion-selective organic electrochemical transistors," *Advanced Materials*, vol. 26, no. 28, pp. 4803–4807, 2014. DOI: 10.1002/adma.201400731.

[25] R. M. Owens, S. Daniel, A. M. Pappa, *et al.*, "Optical and electronic ion channel monitoring from native human membranes," *ACS Nano*, vol. 14, no. 10, 2020. DOI: 10.1021/acsnano.0c01330.

[26] T. Arbring Sjöström, M. Berggren, E. O. Gabrielsson, *et al.*, "A Decade of Iontronic Delivery Devices," *Advanced Materials Technologies*, vol. 3, no. 5, 2018. DOI: 10.1002/admt.201700360.

[27] A. J. Bard, L. R. Faulkner, and H. S. White, *Electrochemical methods: fundamentals and applications*, 2nd ed. John Wiley & Sons Inc., 2001, ISBN: 9780471043720.

[28] K. Tybrandt, I. V. Zozoulenko, and M. Berggren, "Chemical potential–electric double layer coupling in conjugated polymer–polyelectrolyte blends," *Science advances*, vol. 3, no. 12, eaao3659, 2017. DOI: 10.1126/sciadv.aao3659.

[29] K. Tybrandt, "Exploring the potential of ionic bipolar diodes for chemical neural interfaces," *Soft Matter*, vol. 13, no. 44, 2017. DOI: 10.1039/c7sm01732d.

[30] T. A. Sjöström, A. Jonsson, E. O. Gabrielsson, M. Berggren, D. T. Simon, and K. Tybrandt, "Miniaturized Ionic Polarization Diodes for Neurotransmitter Release at Synaptic Speeds," *Advanced Materials Technologies*, vol. 5, no. 3, 2020. DOI: 10.1002/admt.201900750.

[31] T. Arbring Sjöström, A. I. Ivanov, C. Bernard, *et al.*, "Design and Operation of Hybrid Microfluidic Iontronic Probes for Regulated Drug Delivery," *Advanced Materials Technologies*, vol. 6, no. 2, 2021. DOI: 10.1002/admt.202001006.

[32] M. T. Flavin, M. A. Paul, A. S. Lim, *et al.*, "Electrochemical modulation enhances the selectivity of peripheral neurostimulation in vivo," *Proceedings of the National Academy of Sciences*, vol. 119, no. 23, Jun. 2022. DOI: 10.1073/PNAS.2117764119.

[33] S. Romeni, G. Valle, A. Mazzoni, and S. Micera, "Tutorial: a computational framework for the design and optimization of peripheral neural interfaces," *Nature Protocols*, vol. 15, no. 10, 2020. DOI: 10.1038/s41596-020-0377-6.

[34] A. Fellner, A. Heshmat, P. Werginz, and F. Rattay, "A finite element method framework to model extracellular neural stimulation," *Journal of Neural Engineering*, vol. 19, no. 2, p. 022 001, Apr. 2022. DOI: 10.1088/1741-2552/AC6060.

[35] R. Plonsey and R. C. Barr, *Bioelectricity: A quantitative approach*. Springer, 2007, ISBN: 9780387488646. DOI: 10.1007/978-0-387-48865-3.

[36] D. Sterratt, B. Graham, A. Gillies, and D. Willshaw, *Principles of computational modelling in neuroscience*. Cambridge University Press, 2011. DOI: 10.1017/CBO9780511975899.

[37] H. Lindén, E. Hagen, S. Łeski, E. S. Norheim, K. H. Pettersen, and G. T. Einevoll, "LFPy: A tool for biophysical simulation of extracellular potentials generated by detailed model neurons," *Frontiers in Neuroinformatics*, vol. 7, no. JAN, 2014. DOI: 10.3389/fninf.2013.00041.

[38] C. H. Lubba, Y. Le Guen, S. Jarvis, *et al.*, "PyPNS: Multiscale Simulation of a Peripheral Nerve in Python," *Neuroinformatics*, vol. 17, no. 1, 2019. DOI: 10.1007/s12021-018-9383-z.

[39] J. Pods, J. Schönke, and P. Bastian, "Electrodiffusion models of neurons and extracellular space using the poisson-nernst-planck equations - Numerical simulation of the intra- and extracellular potential for an axon model," *Biophysical Journal*, vol. 105, no. 1, 2013. DOI: 10.1016/j.bpj.2013.05.041.

[40] C. L. Lopreore, T. M. Bartol, J. S. Coggan, *et al.*, "Computational modeling of three-dimensional electrodiffusion in biological systems: Application to the node of Ranvier," *Biophysical Journal*, vol. 95, no. 6, 2008. DOI: 10.1529/biophysj.108.132167.

[41] D. Holcman and R. Yuste, "The new nanophysiology: Regulation of ionic flow in neuronal subcompartments," *Nature Reviews Neuroscience*, vol. 16, no. 11, 2015. DOI: 10.1038/nrn4022.

[42] L. P. Savtchenko, M. M. Poo, and D. A. Rusakov, "Electrodiffusion phenomena in neuroscience: A neglected companion," *Nature Reviews Neuroscience*, vol. 18, no. 10, 2017. DOI: 10.1038/nrn.2017.101.

[43] J. R. Cressman, G. Ullah, J. Ziburkus, S. J. Schiff, and E. Barreto, "The influence of sodium and potassium dynamics on excitability, seizures, and the stability of persistent states: I. single neuron dynamics," *Journal of computational neuroscience*, vol. 26, no. 2, pp. 159–170, 2009. DOI: 10.1007/s10827-008-0132-4.

[44] E. Barreto and J. R. Cressman, "Ion concentration dynamics as a mechanism for neuronal bursting," *Journal of Biological Physics*, vol. 37, no. 3, 2011. DOI: 10.1007/s10867-010-9212-6.

[45] Y. Wei, G. Ullah, and S. J. Schiff, "Unification of neuronal spikes, seizures, and spreading depression," *Journal of Neuroscience*, vol. 34, no. 35, 2014. DOI: 10.1523/JNEUROSCI.0516-14.2014.

[46] M. Kalia, H. G. Meijer, S. A. van Gils, M. J. van Putten, and C. R. Rose, "Ion dynamics at the energy-deprived tripartite synapse," *PLoS Computational Biology*, vol. 17, no. 6, 2021. DOI: 10.1371/journal.pcbi.1009019.

[47] S. A. Contreras, J. H. Schleimer, A. T. Gulledge, and S. Schreiber, "Activity-mediated accumulation of potassium induces a switch in firing pattern and neuronal excitability type," *PLoS Computational Biology*, vol. 17, no. 5, 2021. DOI: 10.1371/journal.pcbi.1008510.

[48] H. Kager, W. J. Wadman, and G. G. Somjen, "Simulated seizures and spreading depression in a neuron model incorporating interstitial space and ion concentrations," *Journal of Neurophysiology*, vol. 84, no. 1, 2000. DOI: 10.1152/jn.2000.84.1.495.

[49] *Comsol multiphysics user manual*, COMSOL Inc., Sweden, 2022.

[50] G. Ullah and S. J. Schiff, "Assimilating seizure dynamics," *PLoS Computational Biology*, vol. 6, no. 5, 2010. DOI: 10.1371/journal.pcbi.1000776.

[51] Y. Wei, G. Ullah, J. Ingram, and S. J. Schiff, "Oxygen and seizure dynamics: II. Computational modeling," *Journal of Neurophysiology*, vol. 112, no. 2, 2014. DOI: 10.1152/jn.00541.2013.

[52] A. L. Hodgkin and A. F. Huxley, "A quantitative description of membrane current and its application to conduction and excitation in nerve," *The Journal of Physiology*, vol. 117, no. 4, pp. 500–544, Aug. 1952. DOI: 10.1113/jphysiol.1952.sp004764.

[53] J. Rivnay, P. Leleux, M. Ferro, *et al.*, "High-performance transistors for bioelectronics through tuning of channel thickness," *Science Advances*, vol. 1, no. 4, pp. 1–6, 2015. DOI: 10.1126/sciadv.1400251.

[54] A. V. Volkov, K. Wijeratne, E. Mitraka, *et al.*, "Understanding the Capacitance of PEDOT:PSS," *Advanced Functional Materials*, vol. 27, no. 28, pp. 1–10, 2017. DOI: 10.1002/adfm.201700329.

[55] M. O. Bamgbopa, J. Edberg, I. Engquist, M. Berggren, and K. Tybrandt, "Understanding the characteristics of conducting polymer-redox biopolymer supercapacitors," *Journal of Materials Chemistry A*, vol. 7, no. 41, pp. 23 973–23 980, 2019. DOI: 10.1039/c9ta07030c.

[56] J. Ehlich, L. Migliaccio, I. Sahalianov, *et al.*, "Direct measurement of oxygen reduction reactions at neurostimulation electrodes," *Journal of Neural Engineering*, vol. 19, no. 3, 2022. DOI: 10.1088/1741-2552/ac77c0.

[57] L. J. Mele, P. Palestri, M. A. Alam, and L. Selmi, "Selectivity, sensitivity and detection range in ion-selective membrane-based electrochemical potentiometric sensors analyzed with poisson-boltzmann equilibrium model," *IEEE Sensors Journal*, vol. 22, no. 15, pp. 15 010–15 021, 2022. DOI: 10.1109/JSEN.2022.3185168.

[58] M. J. Sætra, G. T. Einevoll, and G. Halnes, "An electrodiffusive neuron-extracellular-glia model for exploring the genesis of slow potentials in the brain," *PLoS Computational Biology*, vol. 17, no. 7, 2021. DOI: 10.1371/journal.pcbi.1008143.

[59] L. J. Mele, C. Verardo, and P. Palestri, "Reproducing capacitive cyclic voltammetric curves by simulation: When are simplified geometries appropriate?" *Electrochemistry Communications*, vol. 142, p. 107 378, 2022. DOI: 10.1016/j.elecom.2022.107378.

[60] M. Bikson, P. J. Hahn, J. E. Fox, and J. G. Jefferys, "Depolarization block of neurons during maintenance of electrographic seizures," *Journal of Neurophysiology*, vol. 90, no. 4, 2003. DOI: 10.1152/jn.00467.2003.

[61] S. Joucla and B. Yvert, "Modeling extracellular electrical neural stimulation: From basic understanding to MEA-based applications," *Journal of Physiology Paris*, vol. 106, no. 3-4, 2012. DOI: 10.1016/j.jphysparis.2011.10.003.

[62] J. K. Krauss, N. Lipsman, T. Aziz, *et al.*, "Technology of deep brain stimulation: current status and future directions," *Nature Reviews Neurology*, vol. 17, no. 2, 2021. DOI: 10.1038/s41582-020-00426-z.

[63] A. Fitchett, S. Mastitskaya, and K. Aristovich, "Selective Neuromodulation of the Vagus Nerve," *Frontiers in Neuroscience*, vol. 15, 2021. DOI: 10.3389/fnins.2021.685872.

[64] J. J. Jasielec, T. Sokalski, R. Filipek, and A. Lewenstam, "Neutral-Carrier Ion-Selective Electrodes Assessed by the Nernst-Planck-Poisson Model," *Analytical Chemistry*, vol. 87, no. 17, 2015. DOI: 10.1021/acs.analchem.5b00065.

[65] K. Neupert-Laves and M. Dobler, "The crystal structure of a k+ complex of valinomycin," *Helvetica chimica acta*, vol. 58, no. 2, pp. 432–442, 1975. DOI: 10.1002/hlca.19750580212.

[66] K. Aihara and G. Matsumoto, "Two stable steady states in the Hodgkin-Huxley axons," *Biophysical Journal*, vol. 41, no. 1, 1983. DOI: 10.1016/S0006-3495(83)84408-7.

[67] D. Bianchi, A. Marasco, A. Limongiello, *et al.*, "On the mechanisms underlying the depolarization block in the spiking dynamics of CA1 pyramidal neurons," *Journal of Computational Neuroscience*, vol. 33, no. 2, 2012. DOI: 10.1007/s10827-012-0383-y.

[68] M. Bianchi, A. De Salvo, M. Asplund, *et al.*, "Poly(3,4-ethylenedioxythiophene)-Based Neural Interfaces for Recording and Stimulation: Fundamental Aspects and In Vivo Applications," *Advanced Science*, vol. 9, no. 12, 2022. DOI: 10.1002/advs.202104701.

[69] A. Williamson, M. Ferro, P. Leleux, *et al.*, "Localized Neuron Stimulation with Organic Electrochemical Transistors on Delaminating Depth Probes," *Advanced Materials*, vol. 27, no. 30, pp. 4405–4410, 2015. DOI: 10.1002/adma.201500218.

[70] A. Jonsson, S. Inal, L. Uguz, *et al.*, "Bioelectronic neural pixel: Chemical stimulation and electrical sensing at the same site," *Proceedings of the National Academy of Sciences of the United States of America*, vol. 113, no. 34, pp. 9440–9445, 2016. DOI: 10.1073/pnas.1604231113.

[71] P. Bühlmann, E. Pretsch, and E. Bakker, "Carrier-based ion-selective electrodes and bulk optodes. 2. Ionophores for potentiometric and optical sensors," *Chemical Reviews*, vol. 98, no. 4, 1998. DOI: 10.1021/cr970113+.

[72] Y. Qin, Y. Mi, and E. Bakker, "Determination of complex formation constants of 18 neutral alkali and alkaline earth metal ionophores in poly(vinyl chloride) sensing membranes plasticized with bis(2-ethylhexyl)sebacate and o-nitrophenyloctylether," *Analytica Chimica Acta*, vol. 421, no. 2, 2000. DOI: 10.1016/S0003-2670(00)01038-2.

[73] A. Esteban-Linares, X. Zhang, H. H. Lee, *et al.*, "Graphene-based microfluidic perforated microelectrode arrays for retinal electrophysiological studies," *Lab on a Chip*, 2023, ISSN: 1473-0189. DOI: 10.1039/D3LC00064H.

[74] F. Leva, C. Verardo, L. J. Mele, P. Palestri, and L. Selmi, "Multiphysics Finite-Element Modeling of the Neuron/Electrode Electrodiffusive Interaction," *2022 IEEE Sensors*, pp. 1–4, Oct. 2022. DOI: 10.1109/SENSORS52175.2022.9967049.

[75] A. Solbrå, A. W. Bergersen, J. van den Brink, A. Malthe-Sørenssen, G. T. Einevoll, and G. Halnes, "A Kirchhoff-Nernst-Planck framework for modeling large scale extracellular electrodiffusion surrounding morphologically detailed neurons," *PLoS Computational Biology*, vol. 14, no. 10, 2018. DOI: 10.1371/journal.pcbi.1006510.

[76] A. J. Ellingsrud, A. Solbrå, G. T. Einevoll, G. Halnes, and M. E. Rognes, "Finite Element Simulation of Ionic Electrodiffusion in Cellular Geometries," *Frontiers in Neuroinformatics*, vol. 14, 2020. DOI: 10.3389/fninf.2020.00011.

[77] A. Tuttle, J. R. Diaz, and Y. Mori, "A computational study on the role of glutamate and NMDA receptors on cortical spreading depression using a multidomain electrodiffusion model," *PLoS Computational Biology*, vol. 15, no. 12, 2019. DOI: 10.1371/journal.pcbi.1007455.

[78] Y. Mori and C. S. Peskin, "A numerical method for cellular electrophysiology based on the electrodiffusion equations with internal boundary conditions at membranes," *Communications in Applied Mathematics and Computational Science*, vol. 4, no. 1, 2009. DOI: 10.2140/camcos.2009.4.85.

[79] T. Lagache, K. Jayant, and R. Yuste, "Electrodiffusion models of synaptic potentials in dendritic spines," *Journal of Computational Neuroscience*, vol. 47, no. 1, 2019. DOI: 10.1007/s10827-019-00725-5.

[80] R. D. Coalson and M. G. Kurnikova, "Poisson-Nernst-Planck theory approach to the calculation of current through biological ion channels," *IEEE Transactions on Nanobioscience*, vol. 4, no. 1, 2005. DOI: 10.1109/TNB.2004.842495.

[81] C. L. Gardner, J. R. Jones, S. M. Baer, and S. M. Crook, "Drift-diffusion simulation of the ephaptic effect in the triad synapse of the retina," *Journal of Computational Neuroscience*, vol. 38, no. 1, 2015. DOI: 10.1007/s10827-014-0531-7.

[82] E. Hay, S. Hill, F. Schürmann, H. Markram, and I. Segev, "Models of neocortical layer 5b pyramidal cells capturing a wide range of dendritic and perisomatic active properties," *PLoS Computational Biology*, vol. 7, no. 7, 2011. DOI: 10.1371/journal.pcbi.1002107.

[83] H. Markram, E. Muller, S. Ramaswamy, *et al.*, "Reconstruction and Simulation of Neocortical Microcircuitry," *Cell*, vol. 163, no. 2, 2015. DOI: 10.1016/j.cell.2015.09.029.

[84] M. J. Sætra, G. T. Einevoll, and G. Halnes, "An electrodiffusive, ion conserving Pinsky-Rinzel model with homeostatic mechanisms," *PLoS Computational Biology*, vol. 16, no. 4, 2020. DOI: 10.1371/journal.pcbi.1007661.

[85] J. Pods, "A comparison of computational models for the extracellular potential of neurons," *Journal of Integrative Neuroscience*, vol. 16, no. 1, 2017. DOI: 10.3233/JIN-170009.

[86] A. Agudelo-Toro and A. Neef, "Computationally efficient simulation of electrical activity at cell membranes interacting with self-generated and externally imposed electric fields," *Journal of Neural Engineering*, vol. 10, no. 2, 2013. DOI: 10.1088/1741-2560/10/2/026019.

[87] S. Joucla, A. Glière, and B. Yvert, "Current approaches to model extracellular electrical neural microstimulation," *Frontiers in Computational Neuroscience*, vol. 8, no. FEB, 2014. DOI: 10.3389/fncom.2014.00013.

[88] N. T. Carnevale and M. L. Hines, *The NEURON book*. Cambridge University Press, 2006. DOI: 10.1017/CBO9780511541612.

[89] R. A. McDougal, T. M. Morse, T. Carnevale, *et al.*, "Twenty years of ModelDB and beyond: building essential modeling tools for the future of neuroscience," *Journal of Computational Neuroscience*, vol. 42, no. 1, 2017. DOI: 10.1007/s10827-016-0623-7.

[90] R. Bestel, U. Van Rienen, C. Thielemann, and R. Appali, "Influence of Neuronal Morphology on the Shape of Extracellular Recordings with Microelectrode Arrays: A Finite Element Analysis," *IEEE Transactions on Biomedical Engineering*, vol. 68, no. 4, 2021. DOI: 10.1109/TBME.2020.3026635.

[91] M. Berggren and G. G. Malliaras, "How conducting polymer electrodes operate," *Science*, vol. 364, no. 6437, 2019. DOI: 10.1126/science.aaw9295.

[92] E. Syková and C. Nicholson, "Diffusion in brain extracellular space," *Physiological Reviews*, vol. 88, no. 4, 2008, ISSN: 00319333. DOI: 10.1152/physrev.00027.2007.

[93] J. R. Buitenweg, W. L. Rutten, and E. Marani, "Modeled channel distributions explain extracellular recordings from cultured neurons sealed to microelectrodes," *IEEE Transactions on Biomedical Engineering*, vol. 49, no. 12, pp. 1580–1590, 2002.

[94] M. Cucchi, D. Parker, E. Stavrinidou, P. Gkoupidenis, and H. Kleemann, "In Liquido Computation with Electrochemical Transistors and Mixed Conductors for Intelligent Bioelectronics," *Advanced Materials*, 2023. DOI: 10.1002/adma.202209516.

# Supplementary material

# Finite-element modeling of neuromodulation via controlled delivery of potassium ions using conductive polymer-coated microelectrodes

**Claudio Verardo, Leandro Julian Mele, Luca Selmi, Pierpaolo Palestri**

This file includes:

- Supplementary Tables S1-S5.
- Supplementary Figures S1-S12.
- Supplementary Note 1: COMSOL implementation details.
- Supplementary Note 2: model verification.
- Supplementary Note 3: reduced ionoCP-ECF model.

**Table S1.** Abbreviations used in the text.

| Symbol | Description |
|---|---|
| FEM | Finite-element model |
| CP | Conductive polymer |
| isCP | Ideally-selective CP |
| nsCP | Non-selective CP |
| ionoCP | Ionophores-induced selective CP |
| PEDOT-PSS | poly(3,4-ethylenedioxythiophene) polystyrene sulfonate |
| OMIEC | Organic mixed ionic-electronic conductors |
| PNP | Poisson-Nernst-Planck |
| KNP | Kirchhoff-Nernst-Planck |
| ICF | Intracellular fluid |
| ECF | Extracellular fluid |
| AP | Action potential |
| HH | Hodgkin-Huxley |
| EDL | Electrical double layer |
| ORR | Oxygen reduction reactions |
| AMPA | α-amino-3-hydroxy-5-methyl-4-isoxazolepropionic receptor |
| EPSC | Excitatory postsynaptic current |
| WE | Working electrode |
| RE | Reference electrode |
| CE | Counter electrode |
| MEA | Multielectrode array |

**Table S2.** Physical variables solved in the model (Figs. 1, 2 in the main body).

| Symbol | Description | Domain of definition | | | | Units |
|---|---|---|---|---|---|---|
| | | ECF | ICF | Neural Membrane | CP | |
| $\psi_c$ | electric potential (ions) | ✓ | ✓ | | ✓ | mV |
| $\psi_p$ | electric potential (holes) | | | | ✓ | mV |
| $[K^+]$ | $K^+$ concentration | ✓ | ✓ | | ✓ | mM |
| $[Na^+]$ | $Na^+$ concentration | ✓ | ✓ | | ✓ | mM |
| $[Cl^-]$ | $Cl^-$ concentration | ✓ | ✓ | | ✓ | mM |
| $p$ | holes concentration | | | | ✓ | mM |
| $f_K$ | $K^+$ flux | ✓ | ✓ | | ✓ | mol/(m$^2$s) |
| $f_{Na}$ | $Na^+$ flux | ✓ | ✓ | | ✓ | mol/(m$^2$s) |
| $f_{Cl}$ | $Cl^-$ flux | ✓ | ✓ | | ✓ | mol/(m$^2$s) |
| $f_p$ | holes flux | | | | ✓ | mol/(m$^2$s) |
| $V_{app}$ | potential applied to the PEDOT contact | | | | ✓ | V |
| $V$ | membrane potential | | | ✓ | | mV |
| $V_K$ | $K^+$ reversal potential | | | ✓ | | mV |
| $V_{Na}$ | $Na^+$ reversal potential | | | ✓ | | mV |
| $V_{Cl}$ | $Cl^-$ reversal potential | | | ✓ | | mV |
| $I_{K,DR}$ | current $K^+$ voltage-gated channel | | | ✓ | | $\mu$A/cm$^2$ |
| $I_{Na,T}$ | current $Na^+$ voltage-gated channel | | | ✓ | | $\mu$A/cm$^2$ |
| $I_{K,L}$ | current $K^+$ leakage channel | | | ✓ | | $\mu$A/cm$^2$ |
| $I_{Na,L}$ | current $Na^+$ leakage channel | | | ✓ | | $\mu$A/cm$^2$ |
| $I_{Cl,L}$ | current $Cl^-$ leakage channel | | | ✓ | | $\mu$A/cm$^2$ |
| $I_K$ | total current $K^+$ channels | | | ✓ | | $\mu$A/cm$^2$ |
| $I_{Na}$ | total current $Na^+$ channels | | | ✓ | | $\mu$A/cm$^2$ |
| $I_{Cl}$ | total current $Cl^-$ channels | | | ✓ | | $\mu$A/cm$^2$ |
| $n$ | $I_{K,DR}$ activating gating variable | | | ✓ | | - |
| $m$ | $I_{Na,T}$ activating gating variable | | | ✓ | | - |
| $h$ | $I_{Na,T}$ inactivating gating variable | | | ✓ | | - |
| [L] | concentration of free ionophores | | | | ✓ | mM |
| [KL] | concentration of ionophores bound to $K^+$ ions | | | | ✓ | mM |
| $f_L$ | L flux | | | | ✓ | mol/(m$^2$s) |
| $f_{KL}$ | KL flux | | | | ✓ | mol/(m$^2$s) |
| $I_{K,syn}$ | $K^+$ current through AMPA synapse | | | ✓ | | $\mu$A/cm$^2$ |
| $I_{Na,syn}$ | $Na^+$ current through AMPA synapse | | | ✓ | | $\mu$A/cm$^2$ |

**Table S3.** Physical parameters and reference values used in the model (Figs. 1, 2 in the main body).

| Symbol | Description | Value/expression | | | Units | Ref. |
|---|---|---|---|---|---|---|
| | | ECF | ICF | CP | | |
| $T$ | temperature | 309.15 | 309.15 | 309.15 | K | [1] |
| $RT/F$ | thermal voltage | 26.64 | 26.64 | 26.64 | mV | [1] |
| $\varepsilon_{\mathrm{el}}$ | cellular fluids dielectric constant | $80\varepsilon_0$ | $80\varepsilon_0$ | - | F/m | |
| $\varepsilon_{\mathrm{PSS}}$ | dielectric constant PSS phase | - | - | $80\varepsilon_0$ | F/m | |
| $\varepsilon_{\mathrm{PEDOT}}$ | dielectric constant PEDOT phase | - | - | $40\varepsilon_0$ | F/m | [2] |
| $z_{\mathrm{K}}$ | $K^+$ ion valence | +1 | +1 | +1 | - | |
| $z_{\mathrm{Na}}$ | $Na^+$ ion valence | +1 | +1 | +1 | - | |
| $z_{\mathrm{Cl}}$ | $Cl^-$ ion valence | −1 | −1 | −1 | - | |
| $D_{\mathrm{K}}$ | $K^+$ ion diffusivity | $2.19 \cdot 10^{-9}$ | $2.19 \cdot 10^{-9}$ | $5.08 \cdot 10^{-10}$ | $m^2/s$ | [3], [4] |
| $D_{\mathrm{Na}}$ | $Na^+$ ion diffusivity | $1.50 \cdot 10^{-9}$ | $1.50 \cdot 10^{-9}$ | $3.34 \cdot 10^{-10}$ | $m^2/s$ | [3], [4] |
| $D_{\mathrm{Cl}}$ | $Cl^-$ ion diffusivity | $2.28 \cdot 10^{-9}$ | $2.28 \cdot 10^{-9}$ | $5.08 \cdot 10^{-10}$ | $m^2/s$ | [3], [4] |
| $D_p$ | holes diffusivity | - | - | $D_p(p)$ [a] | $m^2/s$ | [4] |
| $[K^+]_{\mathrm{B}}$ | $K^+$ bulk concentration | 4 | 140 | - | mM | [1] |
| $[Na^+]_{\mathrm{B}}$ | $Na^+$ bulk concentration | 144 | 18 | - | mM | [1] |
| $[Cl^-]_{\mathrm{B}}$ | $Cl^-$ bulk concentration | 130 | 6 | - | mM | [1] |
| $[A^-]$ | organic anion concentration | 18 [b] | 152 [b] | - | mM | |
| $[PSS^-]$ | PSS fixed charges (polyanion) | - | - | Table S4 | mM | [4] |
| $C_{\mathrm{V}}$ | volumetric capacitance | - | - | 39 | $F/cm^3$ | [5] |
| $B$ | Au-Ag/AgCl workfunction difference | - | - | −0.7 | V | [4] |
| $\gamma_{\mathrm{K}}$ | CP-ECF virtual selectivity to $K^+$ | - | - | 1 | - | |
| $\gamma_{\mathrm{Na}}$ | CP-ECF virtual selectivity to $Na^+$ | - | - | Table S4 | - | |
| $\gamma_{\mathrm{Cl}}$ | CP-ECF virtual selectivity to $Cl^-$ | - | - | 1 | - | |
| $L_{\mathrm{D}}$ | Debye length | 0.8 [c] | 1.1 [c] | - | nm | [3] |
| $z_{\mathrm{L}}$ | L valence | - | - | 0 | - | |
| $z_{\mathrm{KL}}$ | KL valence | - | - | +1 | - | |
| $D_{\mathrm{L}}$ | L diffusivity | - | - | $D_{\mathrm{K}}/100$ | $m^2/s$ | |
| $D_{\mathrm{KL}}$ | KL diffusivity | - | - | $D_{\mathrm{K}}/100$ | $m^2/s$ | |
| $\beta_{\mathrm{KL}}$ | association constant $K^+$-L binding | - | - | 100 | 1/M | |
| $k_{\mathrm{KL,b}}$ | backward rate constant $K^+$-L binding | - | - | $10^4$ | 1/s | [6] |
| $k_{\mathrm{KL,f}}$ | forward rate constant $K^+$-L binding | - | - | $k_{\mathrm{KL,b}} \cdot \beta_{\mathrm{KL}}$ | 1/(M s) | |
| $[L]_{\mathrm{tot}}$ | total concentration of L and KL | - | - | Table S4 | mM | |
| | | Neural Membrane | | | | |
| $C_{\mathrm{m}}$ | membrane capacitance | 1 | | | $\mu F/cm^2$ | [1] |
| $\overline{g}_{\mathrm{K,DR}}$ | $I_{\mathrm{K,DR}}$ max conductance | 40 | | | $mS/cm^2$ | [1] |
| $\overline{g}_{\mathrm{Na,T}}$ | $I_{\mathrm{Na,T}}$ max conductance | 100 | | | $mS/cm^2$ | [1] |
| $\overline{g}_{\mathrm{K,L}}$ | $I_{\mathrm{K,L}}$ conductance | 0.05 | | | $mS/cm^2$ | [1] |
| $\overline{g}_{\mathrm{Na,L}}$ | $I_{\mathrm{Na,L}}$ conductance | 0.0175 | | | $mS/cm^2$ | [1] |
| $\overline{g}_{\mathrm{Cl,L}}$ | $I_{\mathrm{Cl,L}}$ conductance | 0.05 | | | $mS/cm^2$ | [1] |
| $\phi$ | temperature correction factor | 3 | | | - | [1] |
| $\alpha_n$ | $n$ forward rate constant | $\frac{-0.01(V+34)\phi}{\exp(-0.1(V+34))-1}$ | | | $ms^{-1}$ | [1] |
| $\beta_n$ | $n$ backward rate constant | $0.125\phi \exp(-\frac{V+44}{80})$ | | | $ms^{-1}$ | [1] |
| $\alpha_m$ | $m$ forward rate constant | $\frac{-0.1(V+30)\phi}{\exp(-0.1(V+30))-1}$ | | | $ms^{-1}$ | [1] |
| $\beta_m$ | $m$ backward rate constant | $4\phi \exp(-\frac{V+55}{18})$ | | | $ms^{-1}$ | [1] |
| $\alpha_h$ | $h$ forward rate constant | $0.07\phi \exp(-\frac{V+44}{20})$ | | | $ms^{-1}$ | [1] |
| $\beta_h$ | $h$ backward rate constant | $\frac{\phi}{\exp(-0.1(V+14))+1}$ | | | $ms^{-1}$ | [1] |
| $n_\infty$ | $n$ activation curve | $\frac{\alpha_n(V)}{\alpha_n(V)+\beta_n(V)}$ | | | - | [1] |
| $\tau_n$ | $n$ time constant | $\frac{1}{\alpha_n(V)+\beta_n(V)}$ | | | ms | [1] |
| $m_\infty$ | $m$ activation curve | $\frac{\alpha_m(V)}{\alpha_m(V)+\beta_m(V)}$ | | | - | [1] |
| $\tau_m$ | $m$ time constant | $\frac{1}{\alpha_m(V)+\beta_m(V)}$ | | | ms | [1] |
| $h_\infty$ | $h$ inactivation curve | $\frac{\alpha_h(V)}{\alpha_h(V)+\beta_h(V)}$ | | | - | [1] |
| $\tau_h$ | $h$ time constant | $\frac{1}{\alpha_h(V)+\beta_h(V)}$ | | | ms | [1] |
| $V_{\mathrm{r}}$ | resting membrane potential | −67.0 | | | mV | |
| $I_{\mathrm{K,r}}$ | current of $K^+$ channels at rest | $(I_{\mathrm{K,DR}} + I_{\mathrm{K,L}})\vert_{V=V_{\mathrm{r}}} = 1.41$ | | | $\mu A/cm^2$ | |
| $I_{\mathrm{Na,r}}$ | current of $Na^+$ channels at rest | $(I_{\mathrm{Na,T}} + I_{\mathrm{Na,L}})\vert_{V=V_{\mathrm{r}}} = -2.16$ | | | $\mu A/cm^2$ | |
| $I_{\mathrm{Cl,r}}$ | current of $Cl^-$ channels at rest | $(I_{\mathrm{Cl,L}})\vert_{V=V_{\mathrm{r}}} = 0.75$ | | | $\mu A/cm^2$ | |
| $G_{\mathrm{Na,syn}}$ | $Na^+$ total conductance of AMPA synapse | 2.22 | | | nS | |
| $G_{\mathrm{K,syn}}$ | $K^+$ total conductance of AMPA synapse | 4.90 [d] | | | nS | |
| $\overline{g}_{\mathrm{Na,syn}}$ | $Na^+$ conductance of AMPA synapse | $G_{\mathrm{Na,syn}}/A_{\mathrm{neu}} = 0.30$ | | | $mS/cm^2$ | |
| $\overline{g}_{\mathrm{K,syn}}$ | $K^+$ conductance of AMPA synapse | $G_{\mathrm{K,syn}}/A_{\mathrm{neu}} = 0.67$ | | | $mS/cm^2$ | |
| $\tau_{1,\mathrm{syn}}$ | slow time constant of AMPA synapse | 3 | | | ms | [7] |
| $\tau_{2,\mathrm{syn}}$ | fast time constant of AMPA synapse | 1 | | | ms | [7] |

$R$ gas constant, $F$ Faraday constant, $\varepsilon_0$ vacuum dielectric constant.

[a] $D_p(p) = 2.05 \cdot 10^{-5}(1.05 - 1.08/(1 + \exp((p - 71.0)/22.8)))$.

[b] Set to provide electroneutrality in the bulk of ECF/ICS.

[c] $L_{\mathrm{D}} = \sqrt{\varepsilon_{\mathrm{el}} RT \cdot (F^2 \sum_i z_i^2 [\mathrm{X}_i]_{\mathrm{B}})^{-1}}$ with $\mathrm{X}_i \in \{K^+,\ Na^+,\ Cl^-\}$.

[d] Set to have $I_{\mathrm{K,syn}} = 0.5|I_{\mathrm{Na,syn}}|$ at $V = V_{\mathrm{r}}$ as in [7].

**Table S4.** Parameters from Table S3 that are varied in order to instantiate the case studies considered in the main text (see Section 2.2): ideally-selective CP (isCP), non-selective CP (nsCP), ionophores-induced selective CP (ionoCP). We point out that $[\mathrm{L}]_{\mathrm{tot}} = 0$ corresponds to not including ionophores.

| Symbol | Description | Value/expression | | | Units | Ref. |
|---|---|---|---|---|---|---|
| | | isCP | nsCP | ionoCP | | |
| $\gamma_{\mathrm{Na}}$ | CP-ECF virtual selectivity to $Na^+$ | 0 | 1 | 1 | - | |
| $[\mathrm{L}]_{\mathrm{tot}}$ | total concentration of L and KL | 0 | 0 | 200 | mM | |
| $[\mathrm{PSS}^-]$ | PSS fixed charges (polyanion) | 2400 | 2400 | 637 | mM | [4] |

**Table S5.** Geometrical parameters and reference values used in this work (see Fig. 3).

| Symbol | Description | Value | Units |
|---|---|---|---|
| $W_{\mathrm{el}}$ | electrolyte radius | 40 | $\mu$m |
| $H_{\mathrm{el}}$ | electrolyte height | 40 | $\mu$m |
| $W_{\mathrm{p}}$ | pillar radius | 1.5 | $\mu$m |
| $H_{\mathrm{p}}$ | pillar thickness | 750 | nm |
| $d_{\mathrm{pm}}$ | pillar-neuron cleft | 50 | nm |
| $W_{\mathrm{CP}}$ | CP length | 15 | $\mu$m |
| $H_{\mathrm{CP}}$ | CP thickness | 600 | nm |
| $A_{\mathrm{CP}}$ | CP surface area | 905.9 | $\mu\mathrm{m}^2$ |
| $V_{\mathrm{CP}}$ | CP volume | 508.7 | $\mu\mathrm{m}^3$ |
| $d_{\mathrm{m}}$ | membrane thickness | 10 | nm |
| $d_{\mathrm{s}}$ | sampling distance | 6 | nm |
| $W_{\mathrm{neu}}$ | neuron base radius | 10 | $\mu$m |
| $H_{\mathrm{neu}}$ | neuron height | 4.5 | $\mu$m |
| $A_{\mathrm{neu}}$ | neuron surface area | 730.7 | $\mu\mathrm{m}^2$ |
| $V_{\mathrm{neu}}$ | neuron volume | 942.5 | $\mu\mathrm{m}^3$ |
| $d_{\mathrm{nn}}$ | cleft between active and inactive neurons | 541 | nm |
| $d_{\mathrm{CPm}}$ | CP-neuron cleft | 200 | nm |

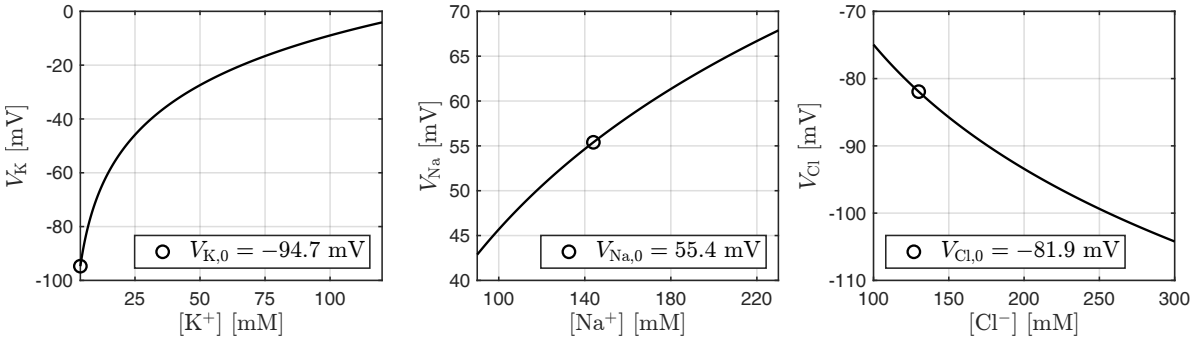



**Figure S1.** Reversal potentials $V_{\mathrm{K}}$, $V_{\mathrm{Na}}$, $V_{\mathrm{Cl}}$ evaluated in ranges of extracellular concentrations considered in the main text, according to the Nernst equation. The intracellular concentrations are kept to their baseline values (see Table S3). The baseline values for the reversal potentials are highlighted with circles. The potassium's reversal potential is the most sensitive to perturbation of the ionic milieu.

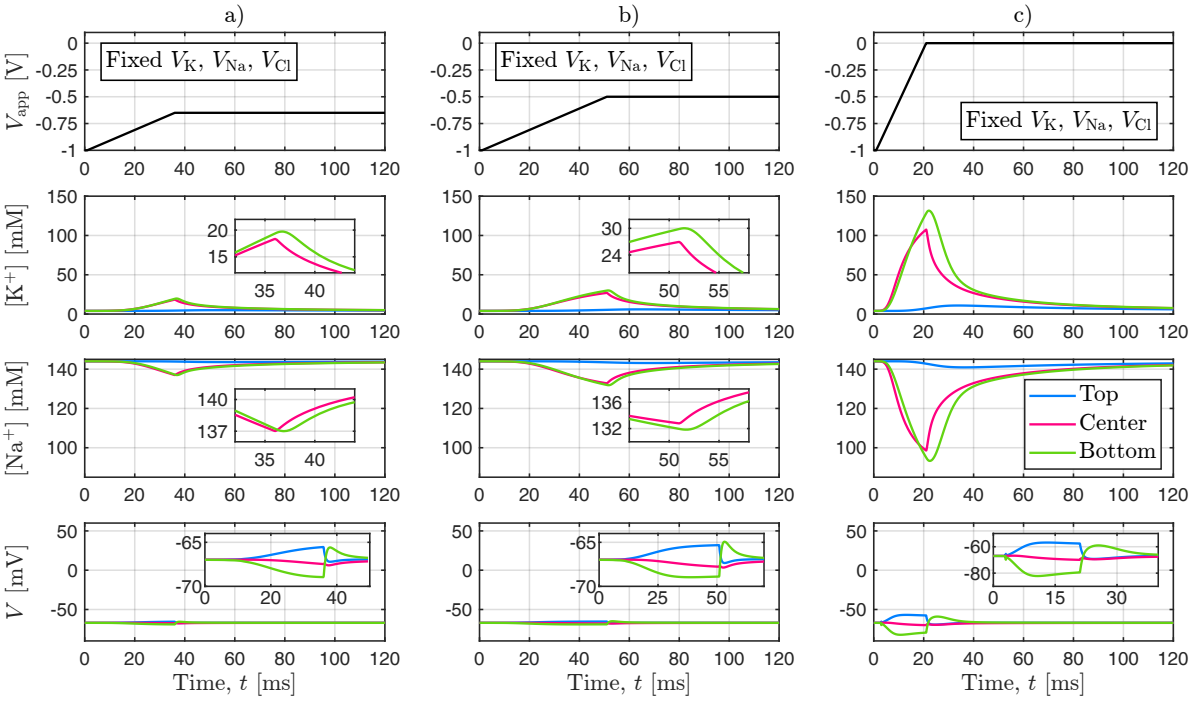



**Figure S2.** Ideally-selective CP (isCP). The same ionic stimulation transients of Fig. 4 are shown but with neuron reversal potentials fixed to their baseline values (see Fig. S1). Sanity check to confirm that the neural activity observed in Fig. 4 is mainly caused by the ionic component of neurostimulation (i.e., the released $K^+$). The hyperpolarization (respectively, depolarization) observed at the bottom (respectively, top) of the neuron are caused by the electric field induced in the ECF during ion release. The extents of such perturbations of membrane potential depend on the slope of the potential applied to the CP (compare columns a), b) with c)). From top to bottom, rows indicate: 1) the applied stimulus $V_{app}$, the extracellular concentrations of 2) [$K^+$] and 3) [$Na^+$] in different points of the ECF and 4) the membrane potential $V$.

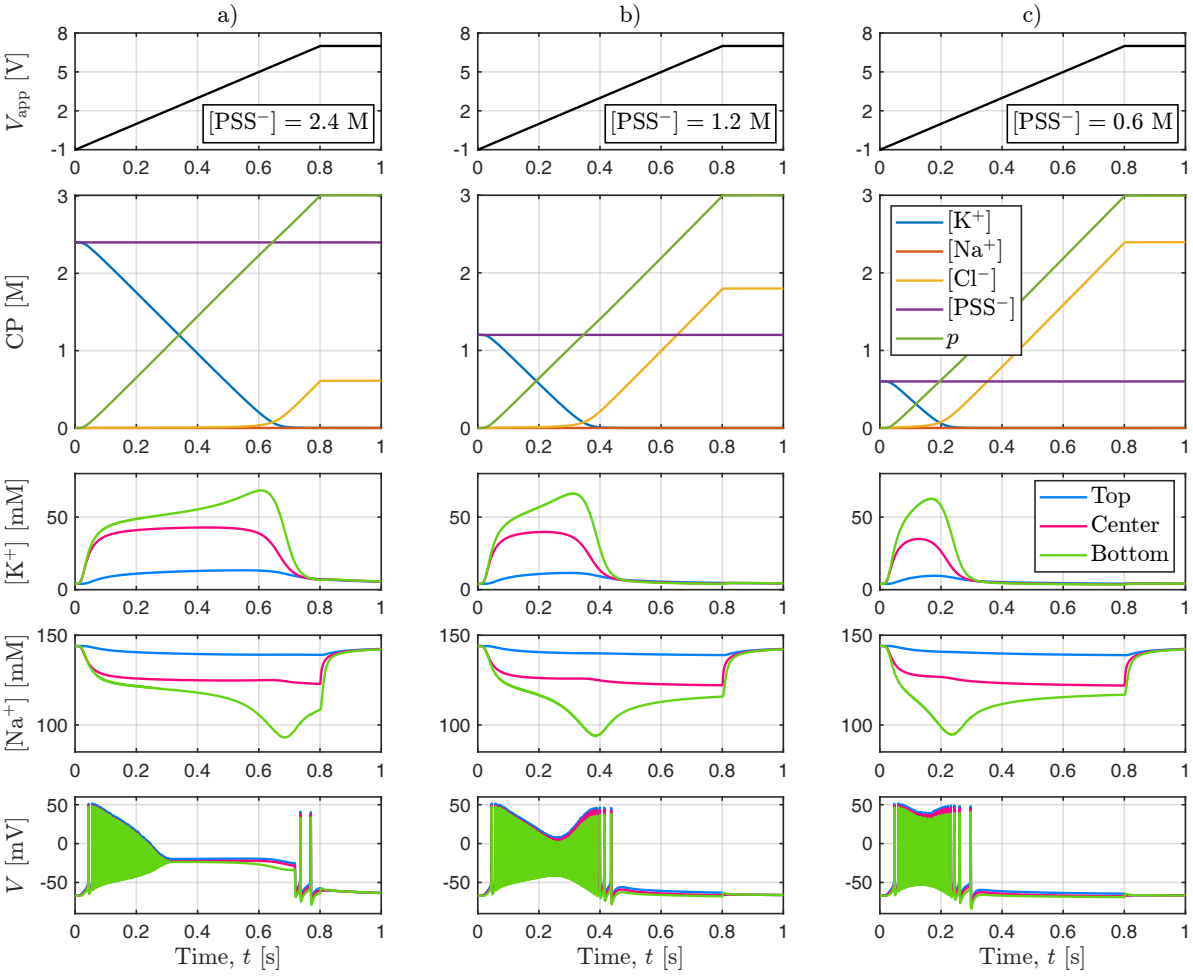



**Figure S3.** Ideally-selective CP (isCP). Examples of ionic stimulation performed with different concentrations of embedded fixed charges in the CP. a) $[PSS^-]$ = 2.4 M (used as reference value as in the main text). b) $[PSS^-]$ = 1.2 M (50% of the reference value). c) $[PSS^-]$ = 0.6 M (25% of the reference value). Compared to Fig. 4, the ramps of applied potential are much longer ($v$ = 10 V/s and $V_{app,max}$ = 7 V) in order to induce a complete depletion of potassium ions in the CP. We observe that higher concentrations of $[PSS^-]$ translate into longer time frames of $K^+$ release. From top to bottom, rows indicate: 1) the applied stimulus $V_{app}$, 2) the ion, hole and fixed charge concentrations inside the CP, the extracellular concentrations of 3) $[K^+]$ and 4) $[Na^+]$ in different points of the ECF, and 5) the membrane potential $V$. Interestingly, with such voltage ramp, larger than those used in the main body of the paper, the neuron response resembles seizure-like events (SLEs), with decreasing APs amplitudes and possible termination in configurations of depolarization block (see last row). The neuron recovers from such SLEs when all the $K^+$ stored in the CP has been released.

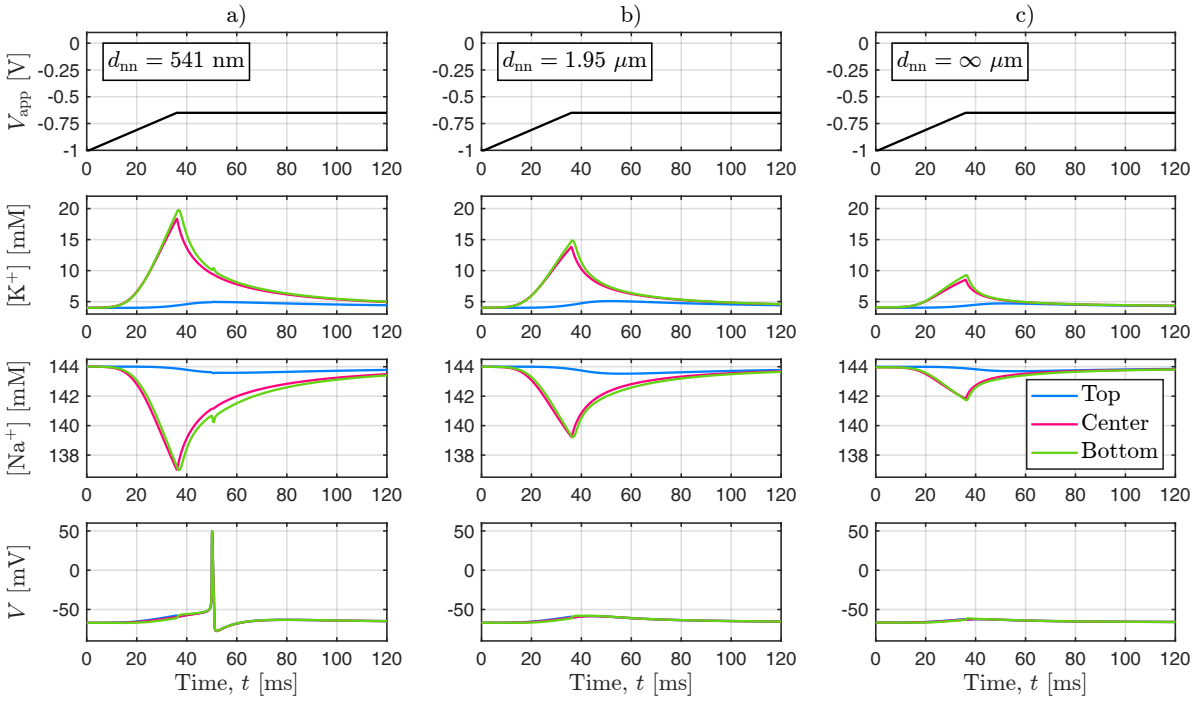



**Figure S4.** Ideally-selective CP (isCP). The ionic stimulation transient of Fig. 4.a is repeated for different extents of neuron's lateral encumbrance. Namely, distances of the lateral inactive neurons $d_{nn}$ (see Fig. 3): a) 541 nm (used as reference value in the main text), b) 1.95 $\mu$m, and c) infinite (i.e., without lateral neurons). Configurations a), and b) correspond to geometries with neuronal area occupation of 90% and 70%, respectively. The area occupation is defined as the ratio between the 2D neuron area $A^{2D}_{neu} = \pi W^2_{neu}$ and the 2D area of its proximal extracellular microenvironment $A^{2D}_{\mu env} = \pi(W_{neu} + d_{nn})^2$, as seen from a top view. Larger occupations of area cause larger perturbations of the local ion concentrations in the ECF, for the same stimulation protocol. From top to bottom, rows indicate: 1) the applied stimulus $V_{app}$, the extracellular concentrations of 2) [K$^+$] and 3) [Na$^+$] in different points of the ECF, and 4) the membrane potential $V$.

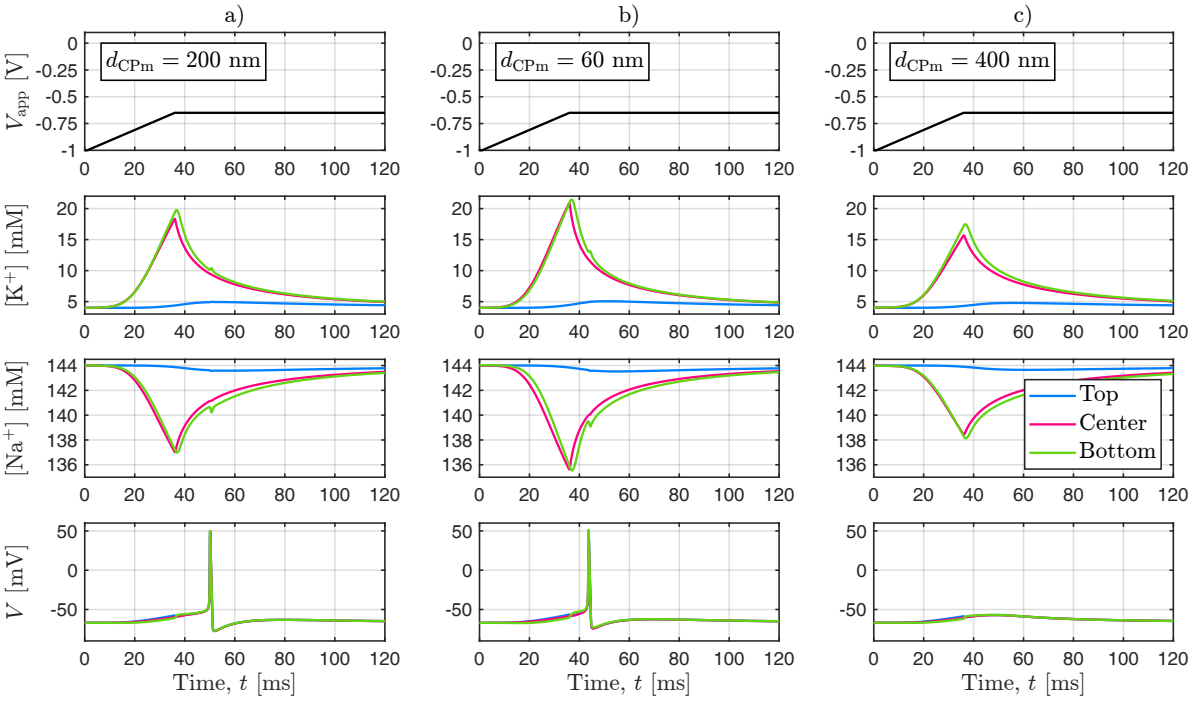



**Figure S5.** Ideally-selective CP (isCP). The ionic stimulation transient of Fig. 4.a is repeated for different extents of the CP-neuron cleft $d_{\mathrm{CPm}}$ (see Fig. 3): a) 200 nm (used as reference value as in the main text), b) 60 nm, and c) 400 nm. A smaller cleft yields a more pronounced perturbation of the local ion concentrations in the ECF, for the same stimulation protocol, which induces a larger depolarization of the neural membrane. The converse applies to a larger cleft. From top to bottom, rows indicate: 1) the applied stimulus $V_{\mathrm{app}}$, the extracellular concentrations of 2) [$\mathrm{K}^+$] and 3) [$\mathrm{Na}^+$] in different points of the ECF, and 4) the membrane potential $V$.

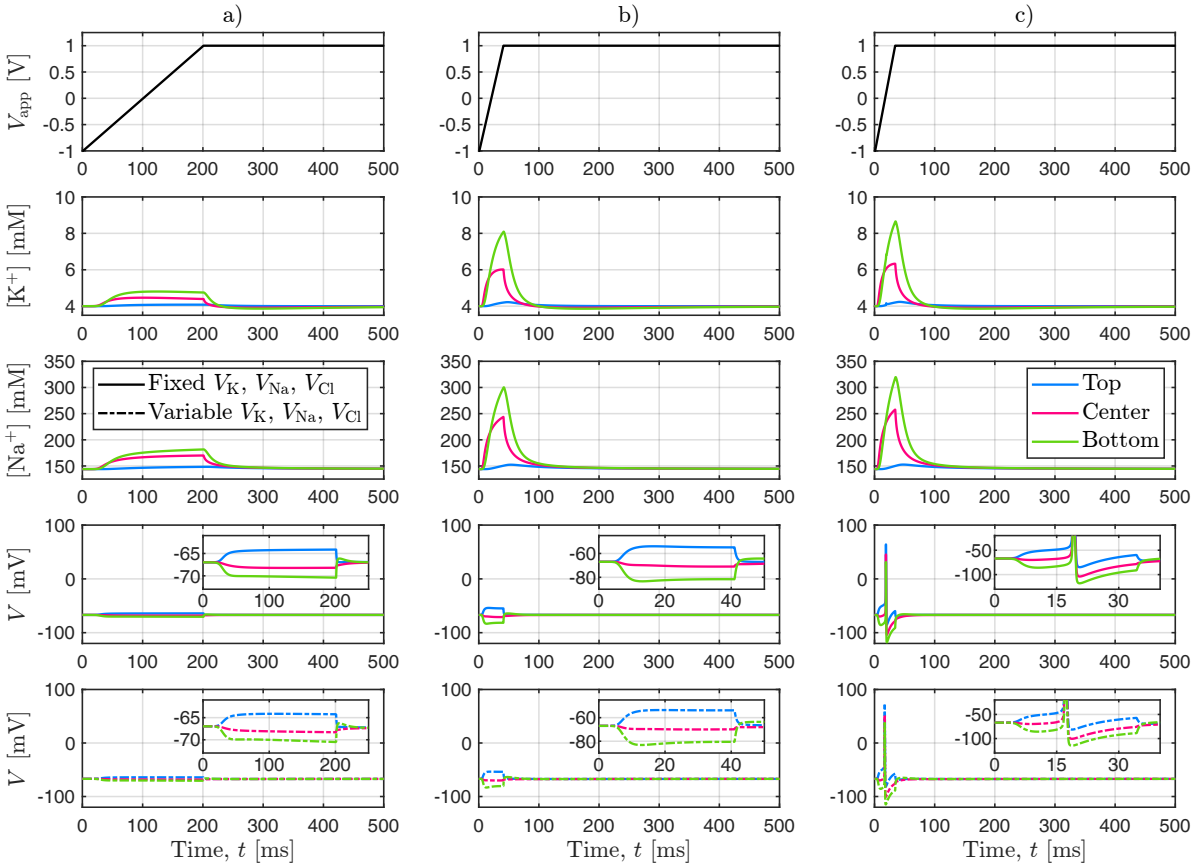



**Figure S6.** Non-selective CP (nsCP). Examples of ionic stimulation transients are performed by keeping either fixed or variable the reversal potentials $V_K$, $V_{Na}$, $V_{Cl}$. Different slopes of the applied potential are considered (with $V_{app,max}$ = 1 V): a) $v$ = 10 V/s (as in Fig. 6.b), b) $v$ = 50 V/s, and c) $v$ = 60 V/s (as in Fig. 6.c). This is a sanity check to confirm that the AP observed in Fig. 6 is mainly caused by the electric component of neurostimulation, rather than the change of the extracellular $Na^+$ and $K^+$ concentrations. From top to bottom, rows indicate: 1) the applied stimulus $V_{app}$, the extracellular concentrations of 2) $[K^+]$ and 3) $[Na^+]$ in different points of the ECF, and the membrane potential $V$ setting 4) fixed or 5) variable reversal potentials during the simulation.

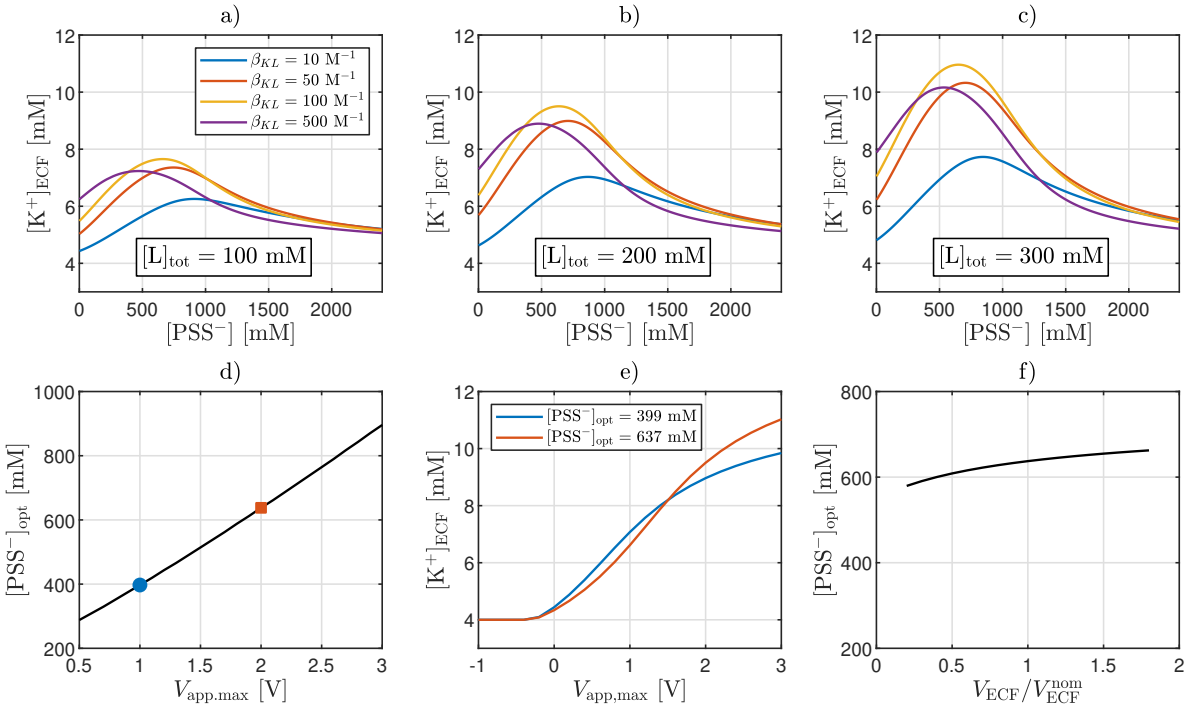



**Figure S7.** Optimizing the ionoCP properties with simulations based on a compartmentalized CP/ECF structure (see Supplementary Note 3). The optimum is evaluated based on the maximum $[K^+]$ change achievable in the ECF for $t \to +\infty$. a-c) $K^+$ vs fixed charge concentrations in the CP for different total concentrations of ionophore $[L]_{tot}$ in the polymer. While larger concentrations of ionophores yield larger release of $K^+$, steric considerations suggest that an upper limit of ca. 200 mM. Interestingly, in all cases the optimum association constant is $\beta_{KL}$ = 100 M$^{-1}$ (green curves). In this work, values as in (b) were used ($[PSS^-] \approx 637$ mM). Further analysis regarding the maximum voltage applied at the CP electrode, $V_{app,max}$, reveals that this parameter impacts the optimum amount of fixed charges (plot (d)). Plot (e) shows that changes of $[PSS^-]$ only slightly impact the ion actuation process, i.e., the change in $[K^+]$ in the extracellular cleft. (f) The choice of the ECF volume does not impact the optimum amount of fixed charges significantly ($V_{ECF}^{nom}$ indicates the nominal value used in (a-e), see Supplementary Note 3).

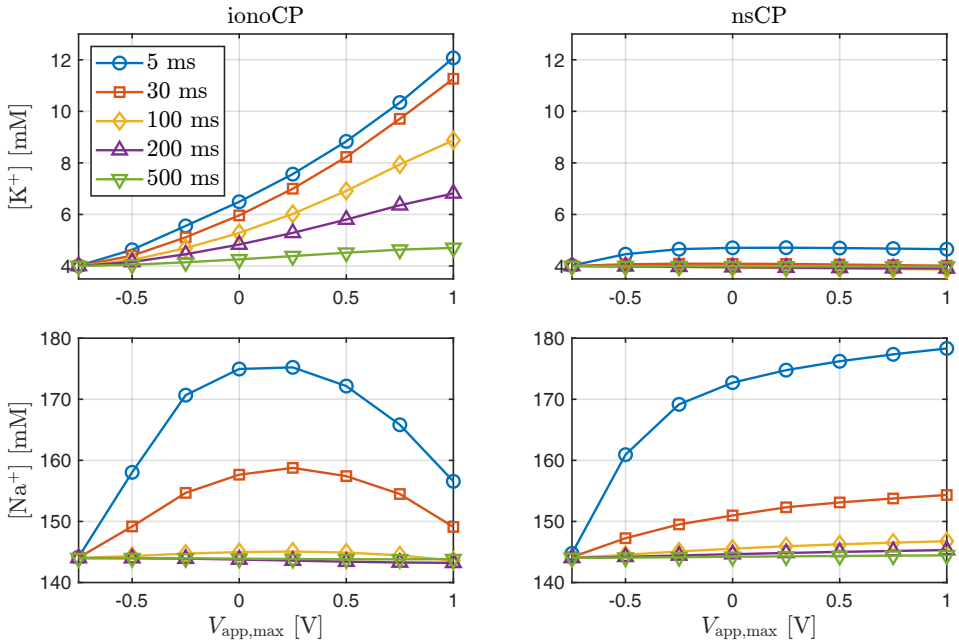



**Figure S8.** Comparison between (left) the ionophores-induced selective CP (ionoCP) and (right) the non-selective CP (nsCP). Simulations of ionic release are performed in both cases with a stimulus $V_{\text{app}}$ with slope $v = 10$ V/s (as in Figs. 7.b and 6.b, respectively). Different values for the maximum applied potential $V_{\text{app,max}}$ are considered. From top to bottom, rows indicate: the concentrations of 1) $K^+$ and 2) $Na^+$ in the cleft between neuron and CP for different $V_{\text{app,max}}$ (markers) and different delays from the end of the $V_{\text{app}}$ ramp (colors). The CP containing ionophores achieve higher $[K^+]$ modulation that persists in time due to the continuing unbinding processes of ionophores until a new equilibrium is reached. The modulation of $[Na^+]$ decays faster in both cases since associated only to sodium drift-diffusion in the ECF (similarly to $K^+$ in the nsCP case). Note that the ratio of the quantity of emitted $K^+$ and $Na^+$ increases with $V_{\text{app,max}}$ in the ionoCP case but not in the nsCP one. This means that the unbinding of ionophore complexes KL is promoted for larger potentials applied to the polymer.

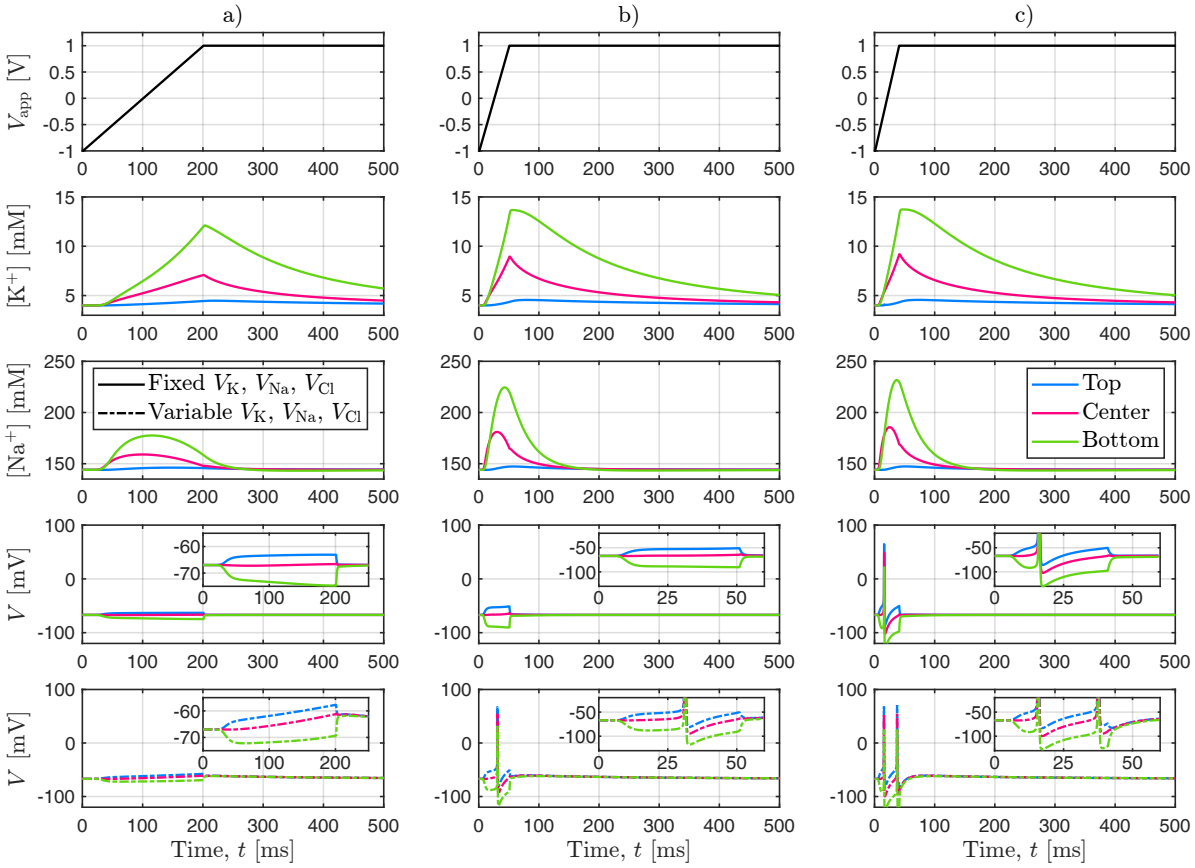



**Figure S9.** Ionophores-induced selective CP (ionoCP). Examples of ionic stimulation transients are performed by keeping either fixed or variable the neuron reversal potentials $V_K$, $V_{Na}$, $V_{Cl}$. Different slopes of the applied potential are considered (with $V_{app,max} = 1$ V): a) $v = 10$ V/s (as in Fig. 7.b), b) $v = 40$ V/s (as in Fig. 7.c), and c) $v = 50$ V/s. This is a sanity check to confirm that the AP observed in Fig. 7 results from both the electric and ionic components of neurostimulation. From top to bottom, rows indicate: 1) the applied stimulus $V_{app}$, the extracellular concentrations of 2) $[K^+]$ and 3) $[Na^+]$ in different points of the ECF, and the membrane potential $V$ elicited with 4) fixed and 5) variable reversal potentials during the simulation.

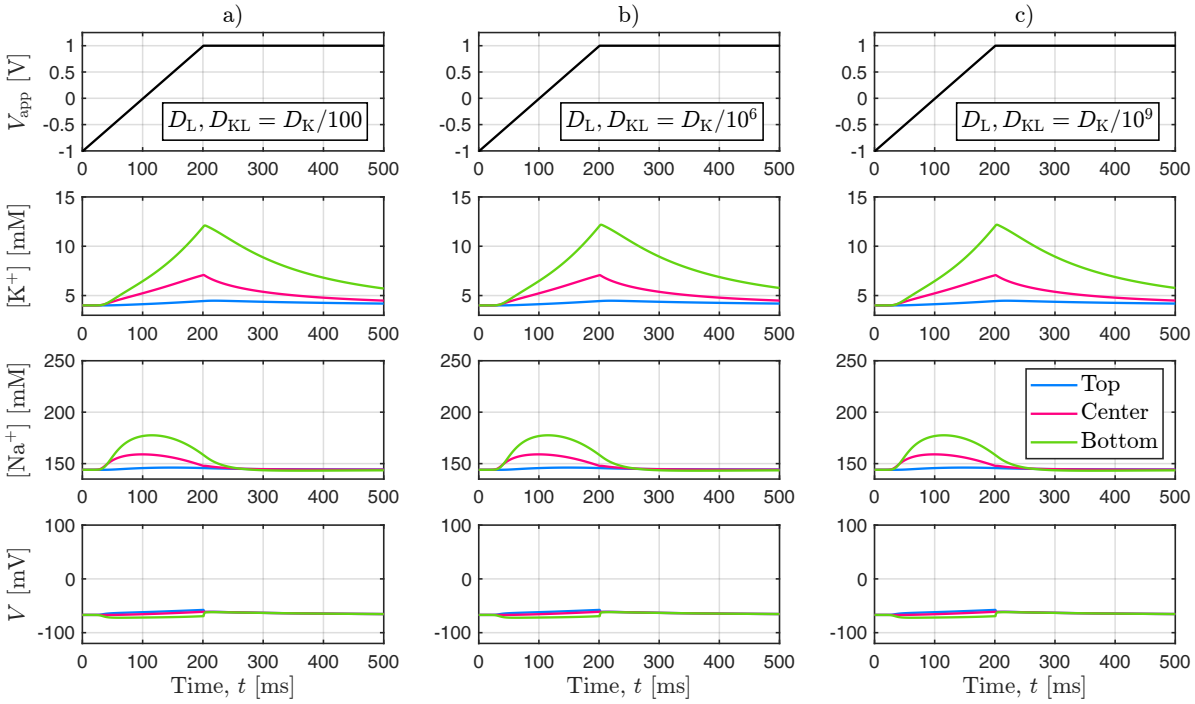



**Figure S10.** Ionophores-induced selective CP (ionoCP). The ionic stimulation transient of Fig. 9.b is shown for different values of the diffusivity coefficient of ionophores. Namely, by reducing them with respect to the one of free $K^+$ by a factor a) 100 (used as reference value as in the main text), b) $10^6$, and c) $10^9$ (fixed ionophore approximation). The results are very mildly affected by this parameter, thereby confirming that the choice of modeling ionophores as mobile rather than fixed species is not critical. From top to bottom, rows indicate: 1) the applied stimulus $V_{app}$, the extracellular concentrations of 2) [$K^+$] and 3) [$Na^+$] in different points of the ECF, and 4) the membrane potential $V$.

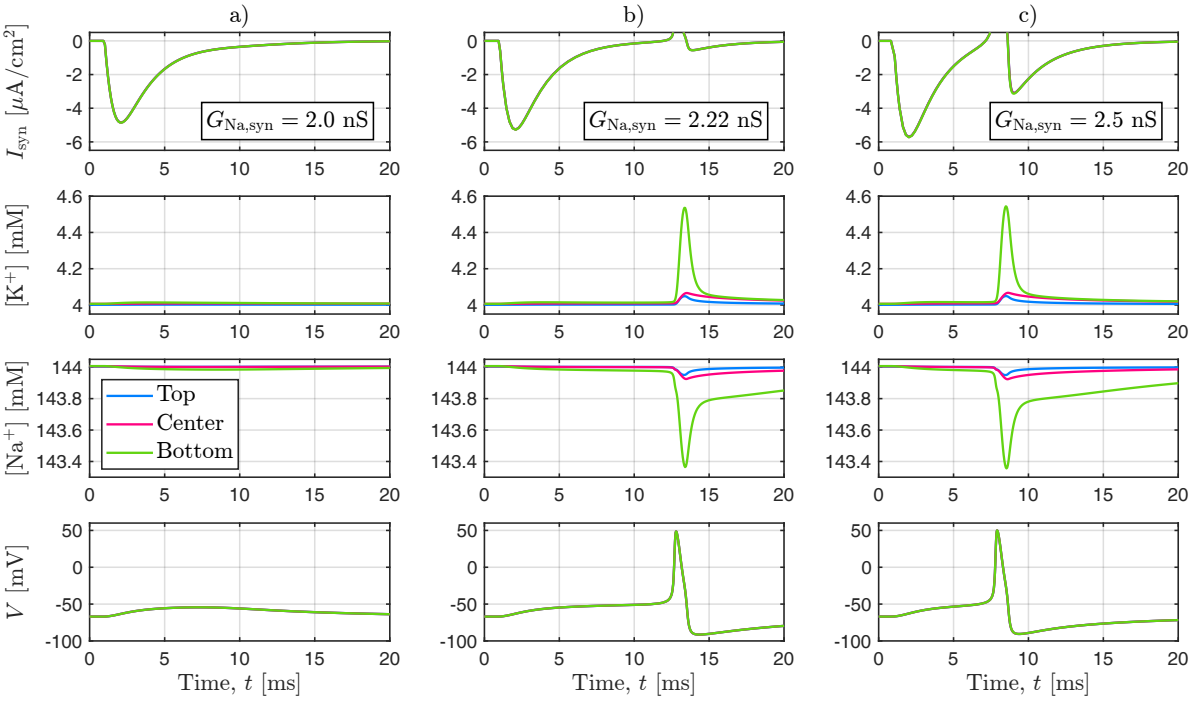



**Figure S11.** Calibration of the total synaptic conductance for sodium $G_{\mathrm{Na,syn}}$ to the threshold to elicit an AP. The potassium one $G_{\mathrm{K,syn}}$ is scaled accordingly (see footnote (d) in Table S3). Note that $G_{\mathrm{Na,syn}}$, $G_{\mathrm{K,syn}}$ are obtained by multiplying the synaptic conductances $g_{\mathrm{Na,syn}}$, $g_{\mathrm{K,syn}}$ mentioned in the main body by the neuronal surface area $A_{\mathrm{neu}}$ (see Table S5), and are adopted for ease of comparison with the original model of the synapse [7]. The CP, assumed ideal, is held at $V_{\mathrm{app}} = -1$ V, hence no ionic release takes place. Three examples of synaptic events are shown for: a) a sub-threshold value $G_{\mathrm{Na,syn}} = 2.0$ nS (no AP elicited), b) the threshold value $G_{\mathrm{Na,syn}} = 2.22$ nS (AP elicited, used in the main body), and c) a supra-threshold value $G_{\mathrm{Na,syn}} = 2.5$ nS (AP elicited earlier than in (b)). The threshold has been found with an accuracy of the 2.2%. From top to bottom, rows indicate: 1) the total synaptic current $I_{\mathrm{syn}} = I_{\mathrm{K,syn}} + I_{\mathrm{Na,syn}}$, the extracellular concentrations of 2) [$K^+$] and 3) [$Na^+$] in different points of the ECF, and 4) the membrane potential $V$.

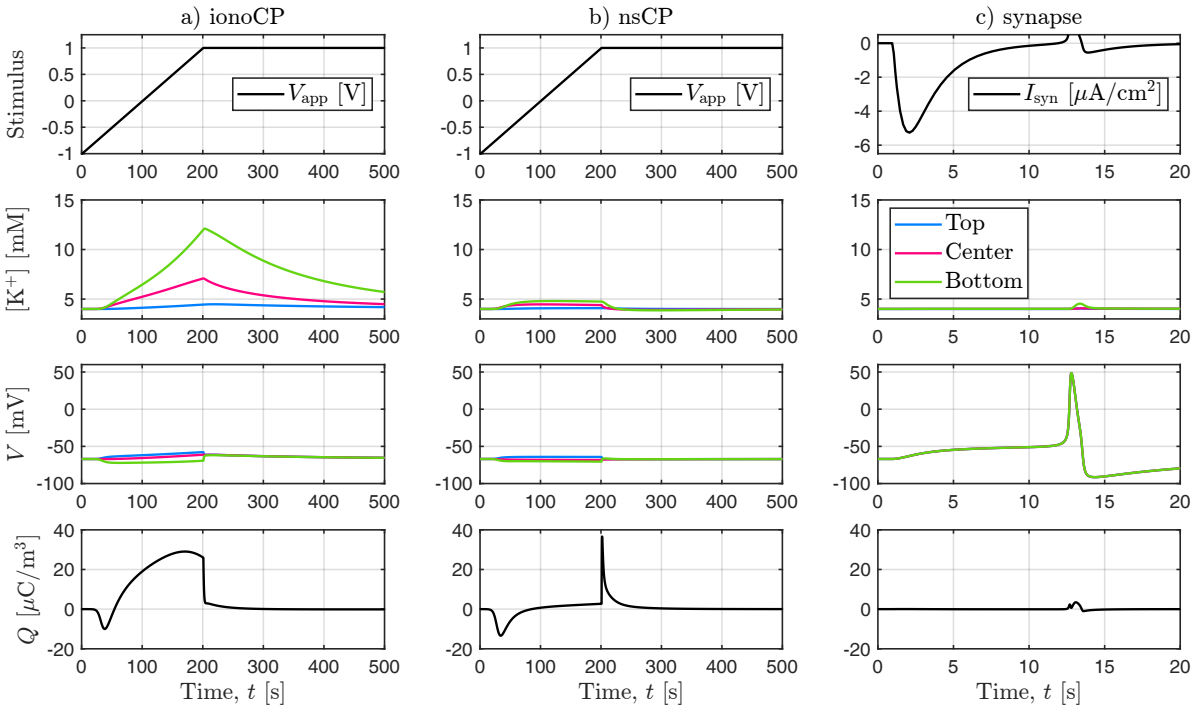



**Figure S12.** Test of electroneutrality in the CP-neuron cleft. Two transients of ionic stimulation are considered for a) the ionophores-induced selective CP (ionoCP) and b) the non-selective CP (nsCP). They are compared to the purely physiological case of synaptic-induced AP in c). We point out that the transients a)-c) correspond to those in Fig. 7.b, Fig. 6.b, and Fig. S11.b, respectively. From top to bottom, rows indicate: 1) the applied stimulus (either the potential applied to the CP, $V_{app}$, or the synaptic current, $I_{syn}$), 2) the extracellular concentration of $[K^+]$, 3) the membrane potential $V$, and 4) the deviation of charged ionic species from electroneutrality in the CP-neuron cleft $Q = F([K^+] + [Na^+] - [Cl^-] - [A^-])$. The charge induced in a) results up to an order of magnitude greater than that in c). The charge in b) is instead comparable to that in c), with the exception of the starting and ending phases of the $V_{app}$ ramp. We also point out that the time scales in a)-b) are much larger than in c), with charge density perturbation lasting hundreds of ms in the former ones while just a few ms in the latter one. These results suggest that the electroneutrality assumption might not be trivially satisfied in the ionoCP case. Only more in-depth investigations and comparisons with the KNP formalism (see Discussion) can better shed light on the problem.

**Supplementary Note 1: COMSOL implementation details**

The model equations reported in Figs. 1, 2 of the main body were implemented using COMSOL Multiphysics v6.0 [8]. For the sake of reproducibility, we herein report the main features adopted in our models.

*Rotational symmetry* To enforce the symmetry around the vertical axis of the geometry (see Fig. 3), the model has been implemented as a *2D Axisymmetric Component*. In such a way, the 3D geometry is defined by its 2D cross-section, and the model equations are automatically adapted to ensure rotational symmetry in the solutions.

*Physical interfaces* PNP models employed for the ICF, ECF and CP were obtained by combining the *Transport of Dilute Species* and *Electrostatic* physical interfaces, that belong to the electrochemistry and AC/DC packages, respectively. Given the peculiar form of the PNP model describing the CP (see Fig. 1 in the main text), we used user-defined variables to handle the coupling between Poisson and continuity equations, instead of the built-in multiphysics features. The HH model was implemented using *Boundary Ordinary Differential Equations (Boundary ODEs)* at the neuron membrane boundaries. Sample points at 6 nm distance inside and outside the cell membrane were made accessible to the HH model for computing the reversal potentials by using *linear extrusion* operators, available among non-local coupling functions. Similar functions were also employed to create a common set of variables at both sides of the membrane boundary.

*Meshing* Meshes were designed using the non-linear *Boundary Layer* mesh-generator with an initial element size of subnanometer length (set using the miminum step size allowed by COMSOL) close to charged interfaces, followed by mesh elements whose size varies exponentially until a maximum predefined size is reached. The number of mesh elements along boundaries was controlled by the *distribution* feature. In the bulk of each simulation domain, the maximum predefined size was set to 1.5 $\mu$m in the ECF, 0.6 $\mu$m in the ICF, and 0.15 $\mu$m in the CP. A convergence analysis was performed to make sure that the selected mesh size provided sufficient accuracy on the results. As shown in Figure S13, a reduction of the maximum element size in the chosen mesh does not induce any change in the solution found by the model.

*Studies* The initial conditions for ionic actuation transients in the isCP and nsCP cases were found through stationary studies. In the ionoCP case, to help convergence, the initial conditions were found via a stationary study with the dynamics of ionophores disabled and followed by a time-dependent study (10 s) of the full model. Ionic actuation transients starting from such initial conditions were simulated through time-dependent studies with *intermediate* time step setting. The results shown in the main text were sampled at the actual time steps taken by the solver using *probes*.

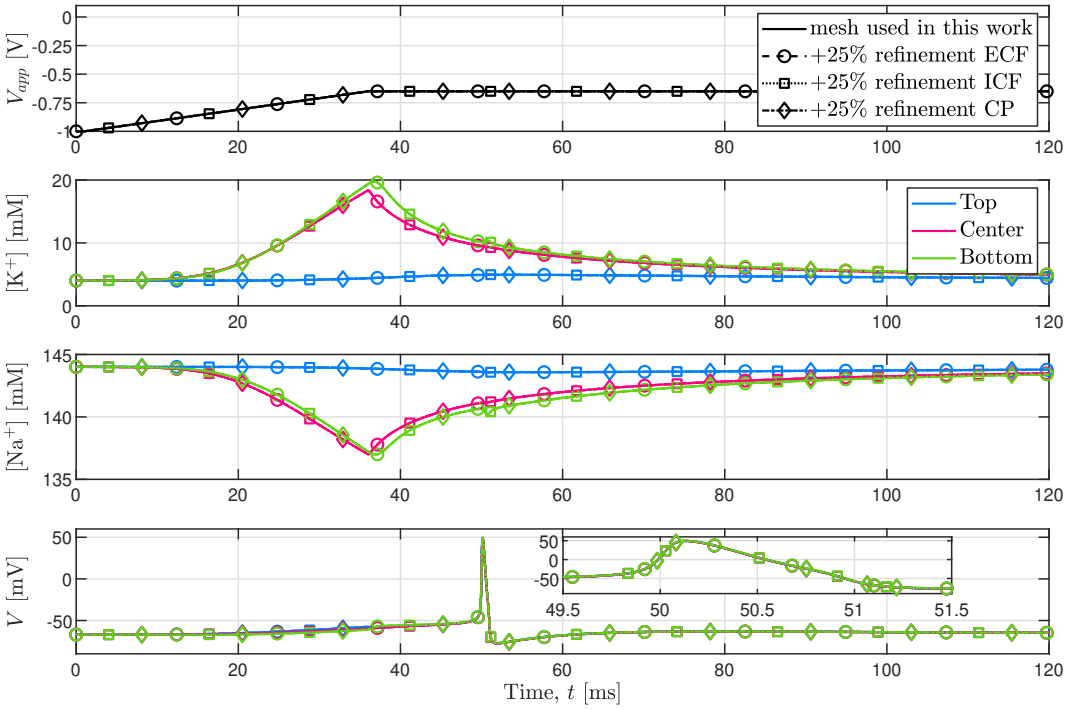



**Figure S13.** Convergence analysis of the mesh used in the work. The transient in Fig. 4.a (here, in solid lines) is repeated after reduction of the 25% of the maximum element size in the ECF (dashed lines), ICF (dotted line), and CP (dashed-dotted line). From top to bottom, rows indicate: 1) the applied stimulus to the CP $V_{\text{app}}$, the extracellular concentration of 2) [$K^+$] and 3) [$Na^+$], and 4) the membrane potential $V$. The results are in perfect agreement (all curves overlap), thereby confirming the appropriate meshing of the system.

*Computational burden* Given the numerical complexity of the modeled problems, we used a cluster of servers to perform simulations. To this aim, we employed the *batch* command-line interface to COMSOL Multyphysics.

To provide a glimpse on the mentioned computational burden, we herein report the computational time for the parameter sweeps in Figs. 9.B and 9.D. For such simulations, two servers with the following specifications were used in parallel:

- Server 1: 2x Intel® Xeon® CPU X5690 at 3.47 GHz (12 cores), 189 GB RAM.
- Server 2: 2x Intel® Xeon® CPU Gold 6136 at 3.00 GHz (24 cores), 500 GB RAM.

Simulations in Fig. 9.B consisted of time-dependent studies lasting 300 ms with a maximum time step of 1 ms. The total solving time was 30:53:03 (hh:mm:ss), with 13:52:22 carried out by Server 1 and 17:00:41 by Server 2. Table S6 reports the times (mm:ss) of each simulation (bold text: Server 1, plain text: Server 2).

Simulations in Fig. 9.D consisted of time-dependent studies lasting 400 ms with a maximum time step of 1 ms. The total solving time was 39:03:26 (hh:mm:ss), with 19:32:55 carried out by Server 1 and 19:30:31 by Server 2. Table S7 reports the times (mm:ss) of each simulation (bold text: Server 1, plain text: Server 2).

**Table S6.** Simulation time of the studies in Fig. 9.B.

| scale $g_{X_i,\mathrm{syn}}$ | $V_{\mathrm{app,max}}$ [V] | | | | | | | |
|---|---|---|---|---|---|---|---|---|
| | -0.75 | -0.50 | -0.25 | 0 | 0.25 | 0.50 | 0.75 | 1.00 |
| 0.9 | **32:37** | **45:54** | **44:46** | 23:52 | 24:50 | 24:12 | 24:18 | 24:20 |
| 0.8 | **32:35** | **35:20** | **45:57** | 23:56 | 23:36 | 23:46 | 23:47 | 24:02 |
| 0.7 | **31:31** | **33:56** | **33:43** | 23:36 | 24:07 | 24:29 | 24:45 | 24:22 |
| 0.6 | **33:21** | **34:14** | **34:11** | 18:16 | 24:36 | 24:34 | 24:23 | 24:08 |
| 0.5 | **31:30** | **34:42** | **33:50** | 18:00 | 18:08 | 24:29 | 24:07 | 23:49 |
| 0.4 | **32:09** | **34:00** | **33:01** | 18:19 | 17:52 | 18:53 | 23:51 | 24:24 |
| 0.3 | **32:00** | **34:04** | 18:07 | 17:45 | 17:48 | 18:09 | 18:24 | 24:28 |
| 0.2 | **31:12** | **33:50** | 17:59 | 17:34 | 18:00 | 18:16 | 18:22 | 18:27 |
| 0.1 | **31:21** | **32:38** | 18:06 | 17:53 | 17:33 | 17:57 | 17:56 | 18:10 |

**Table S7.** Simulation time of the studies in Fig. 9.D.

| scale $g_{X_i,\mathrm{syn}}$ | $V_{\mathrm{app,max}}$ [V] | | | | | | | |
|---|---|---|---|---|---|---|---|---|
| | -0.75 | -0.50 | -0.25 | 0 | 0.25 | 0.50 | 0.75 | 1.00 |
| 0.9 | **41:54** | **44:57** | **55:55** | 28:23 | 28:39 | 29:12 | 29:18 | 29:25 |
| 0.8 | **42:04** | **43:57** | **44:23** | 28:41 | 28:08 | 29:31 | 29:43 | 29:01 |
| 0.7 | **42:08** | **44:33** | **43:27** | 29:30 | 29:15 | 29:53 | 28:56 | 28:52 |
| 0.6 | **42:35** | **43:49** | **43:19** | 23:33 | 23:12 | 30:30 | 28:24 | 30:13 |
| 0.5 | **41:37** | **43:47** | **43:28** | 23:25 | 23:04 | 23:56 | 29:45 | 29:11 |
| 0.4 | **41:44** | **44:12** | **43:54** | 22:39 | 23:23 | 23:31 | 23:05 | 29:52 |
| 0.3 | **41:16** | **43:28** | **43:10** | 23:21 | 22:25 | 23:21 | 23:32 | 23:35 |
| 0.2 | **41:04** | **43:02** | **43:20** | 23:16 | 22:25 | 23:11 | 23:31 | 23:30 |
| 0.1 | **41:29** | **42:04** | **42:19** | 22:52 | 22:48 | 23:03 | 22:37 | 22:54 |

**Supplementary Note 2: model verification**

Given the transient nature of the mechanisms under study, we are interested in time-dependent simulations of the polymer – cellular fluids – neural membrane system (see Fig. 1 in the main text). To the extent of our knowledge, analytical solutions are not available for such scenarios. Therefore, to verify the correct implementation of our model, we considered simplified geometries and limit cases as benchmarks.

*Simplified geometry: AP propagation along an unmyelinated fiber* We reproduced the results of electrodiffusive model for an unmyelinated axon (1 um diameter, 10 mm length) from [9]. Therein, the system was implemented with a formalism very similar to ours (the minor differences are discussed in Sections 2.1.2 - 2.1.3) and solved with a custom software. Figure S14.a shows that our COMSOL implementation reproduces quite closely the propagation of an action potential excited by a 0.965 nA stimulus applied at $t = 0$ for 2 ms (namely, Fig. 2 in [9]). The propagation velocity results 0.90 ms/s instead of 0.93 m/s as in [9]. Notwithstanding, the referenced work does not provide a convergence analysis of the solution. The difference emerges from the finer mesh employed in our model, with a minimum element size of 0.07 nm along the transverse direction (instead of 0.5 nm in [9]) and 5 $\mu$m along the longitudinal direction (instead of 100 $\mu$m in [9]). Indeed, as shown in Fig. S14.b, we find a better agreement by simulating the system with a coarser mesh resembling that of [9]. This analysis confirms the correctness of our implementation of the coupling between the neural membrane and the cellular fluids.

*Limit case: ohmic approximation for cellular fluids* A verification of the entire system (including the conductive polymer) has been carried out considering the limit case of electrical stimulation. This limit case occurs when the perturbation of ionic concentrations in the extracellular fluid during the actuation phase is negligible, and the electric field increase is the main mechanism responsible for generating the action potential. In this case (referred to as *pure electrical stimulation* in the main text), the electrolyte can be effectively modeled as an ohmic conductor, thereby neglecting diffusion currents. This formalism is typically employed to model the interface between neurons and implanted electrodes, both for stimulation [10] and recording [11].

In the ohmic electrolyte approximated model, the PNP equations (Eqs. 1-3 in Fig. 1) are replaced in our COMSOL deck by

$$\nabla \cdot \left( \sigma_{\mathrm{el}} \nabla \psi_c + \varepsilon_{\mathrm{el}} \frac{\partial \nabla \psi_c}{\partial t} \right) = 0, \tag{S1}$$

where $\sigma_{\mathrm{el}}$ is the ionic conductivity, defined as

$$\sigma_{\mathrm{el}} = \frac{F^2}{RT} \left( D_{\mathrm{K}} \left[ \mathrm{K}^+ \right]_{\mathrm{B}} + D_{\mathrm{Na}} \left[ \mathrm{Na}^+ \right]_{\mathrm{B}} + D_{\mathrm{Cl}} \left[ \mathrm{Cl}^- \right]_{\mathrm{B}} \right). \tag{S2}$$

By inserting the parameters values used in Table S3 we obtain $\sigma_{\mathrm{el}} = 1.3$ S/m for the extracellular fluid and $\sigma_{\mathrm{el}} = 2.0$ S/m for the intracellular fluid. While the description of

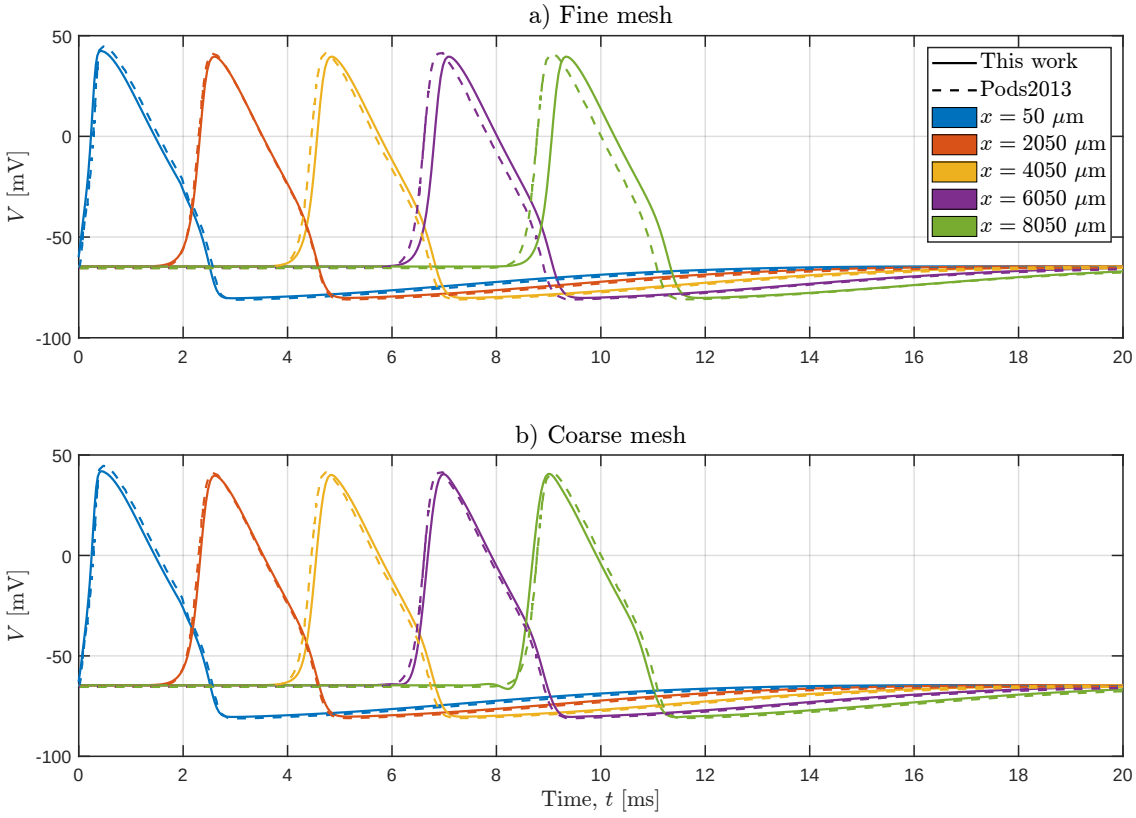



**Figure S14.** Comparison of our model to the electrodiffusive model of unmyelinated axon from [9]. The system is excited by a 0.965 nA stimulus applied at $t = 0$ for 2 ms. The solid lines represent the membrane potential predicted by our model, while the dashed ones are from Fig. 2 in [9]. The $x$ refers to the longitudinal position along the axon where the membrane potential $V$ is sampled. In a) we use a finer mesh than in [9]. In b) we use a coarser mesh resembling the one used in [9].

the neural membrane (HH model) does not change (Eqs. 6-8 in Fig. 1), the boundary conditions that couple the neural membrane and the cellular fluids (Eqs. 4-5, 9-10 in Fig. 1) need to be substituted with

$$\hat{u} \cdot \nabla \psi_c \Big|_{\substack{\text{intra} \\ \text{extra}}} = \mp \left( C_\text{m} \frac{dV}{dt} + I_\text{K} + I_\text{Na} + I_\text{Cl} \right), \tag{S3}$$

$$V = \psi_c \Big|_\text{intra} - \psi_c \Big|_\text{extra}, \tag{S4}$$

where $\hat{u}$ is the vector normal to the membrane surface. In a similar way, the conductive polymer is substituted by a flux boundary condition that injects in the extracellular fluid the same ionic current predicted by the electrodiffusive model (i.e., the PNP model in COMSOL) according to

$$\hat{u} \cdot (\sigma_\text{el} \nabla \psi_c) \Big|_\text{CP} = I_\text{CP} = F \frac{d}{dt} \left( \int_\text{CP} p \; d\Omega \right). \tag{S5}$$

Figure S15 reports the ionic actuation transients obtained with the non-selective CP (nsCP) following either the electrodiffusive or the ohmic formalisms. Two widths of the

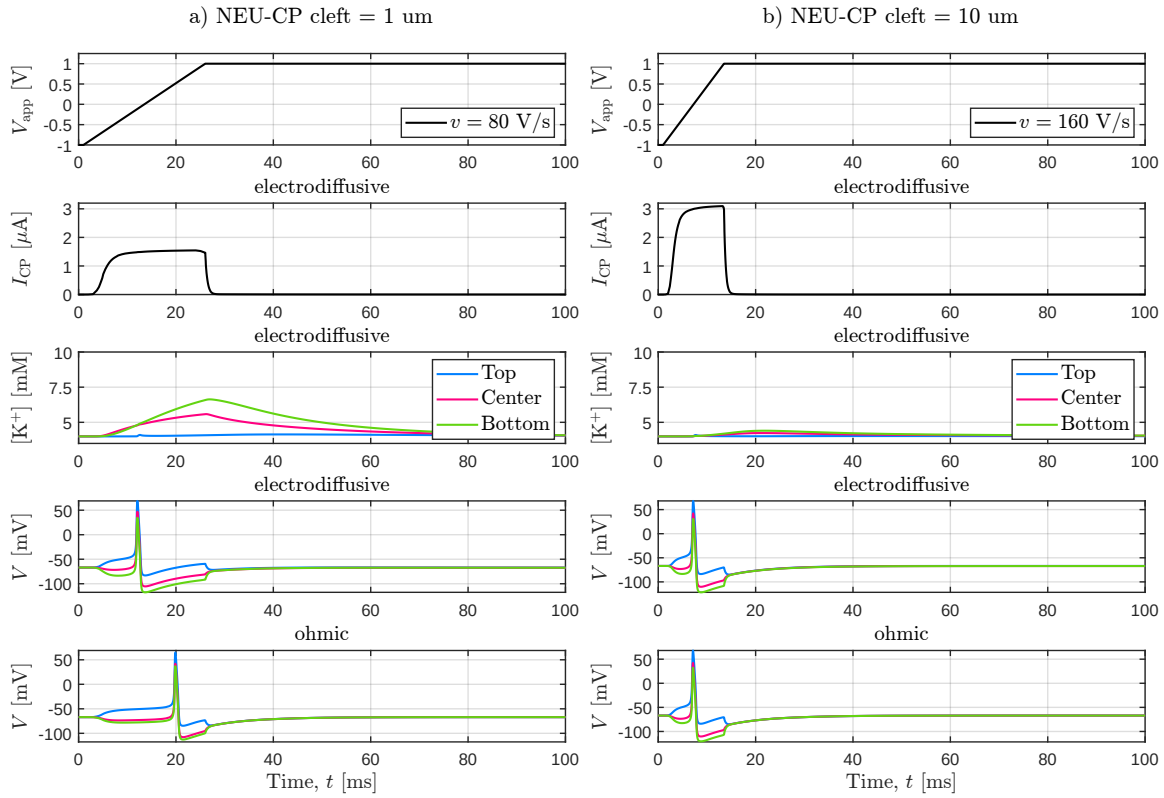



**Figure S15.** Comparison of the predictions of the electrodiffusive and ohmic models during an actuation transient with the non-selective CP (nsCP). The title of each inset denotes the model used to solve the plotted variable. In a) a neuron-CP cleft of 1 um is considered and the two model predictions differ due to the non-negligible change of ionic concentrations. Conversely, in b) a neuron-CP cleft of 10 $\mu$m is considered and the results of the two models are in good mutual agreement.

neuron-CP cleft ($d_{\mathrm{CP_n}}$) are considered: a) 1 $\mu$m and b) 10 $\mu$m. The rows 1-4 of the plots are results from simulations of the electrodiffusive model, while row 5 contains the results from the ohmic model. In a), the perturbation of ionic concentrations is not negligible due to the small size of the neuron-CP cleft. Therefore, the profile of membrane potential predicted by the two models differs. In fact, in this situation, the electrodiffusive description is more general than the ohmic one. In b) the cleft is very large and ionic concentrations are mildly perturbed by the action of the ionic actuator. Therefore, the predictions of the two models are in good agreement, corroborating the correctness of the implementation of our electrodiffusive model (that naturally tends to the ohmic model in the cases where this latter is valid).

**Supplementary Note 3: reduced ionoCP-ECF model**

For the optimization of the ionophores-induced selective CP (ionoCP), we considered a phase-boundary model of the interaction between the ionic actuator and the ECF. Namely, we lumped the CP, CP contact, and ECF in compartments. Further, we considered only the equilibrium state of the system. The model is employed to study, 1), the precharging capacity of the ionoCP and, 2), the subsequent release step (see Section 3.3 and Fig. S7).

**ionoCP precharge**: This model assumes:

(i) Electroneutrality everywhere in the domain.

(ii) Electrodiffusion processes at thermodynamic equilibrium. Namely, concentrations follow Boltzmann distributions

$$[\mathrm{X}_i] = [\mathrm{X}_i]_\mathrm{B}\left(-\frac{z_{\mathrm{X}_i}F}{RT}\exp(\psi_c - \psi_{c,\mathrm{B}})\right) \tag{S6}$$

$$p = p_\mathrm{M}\left(-\frac{F}{RT}\exp(\psi_p - \psi_{p,\mathrm{M}})\right), \tag{S7}$$

where $\mathrm{X}_i \in \{\mathrm{K}^+, \mathrm{Na}^+, \mathrm{Cl}^-\}$. The subscript B denotes the reference point for ionic concentrations and is taken at the bulk of the ECF. The subscript M denotes the reference point for holes and is taken at the CP (metal) contact.

(iii) Chemical reactions (for ionophores) are at thermodynamic equilibrium, i.e., it holds

$$\beta_\mathrm{KL} = \frac{[\mathrm{KL}]}{[\mathrm{K}^+]_\mathrm{CP}[\mathrm{L}]} \tag{S8}$$

(iv) Mass conservation for ionophores:

$$[\mathrm{L}] + [\mathrm{KL}] = [\mathrm{L}]_\mathrm{tot} \tag{S9}$$

We point out that (ii) and (iii) hold true at equilibrium only if ionophores are regarded as fixed species, i.e., their fluxes $f_\mathrm{L}$, $f_\mathrm{KL}$ are null. As seen in the main body, this is not a critical assumption. Hereafter, we summarize the variables solved in the reduced model and those set according to assumption i) ‡.

| Full model | Reduced model | | | Units |
|---|---|---|---|---|
| | CP contact | CP | ECF | |
| $\psi_c$ | - | $\psi_c$ | $\psi_{c,\mathrm{B}} = 0$ | V |
| $\psi_p$ | $\psi_{p,\mathrm{M}} = -1$ | $\psi_p$ | - | V |
| $[\mathrm{K}^+]$ | - | $[\mathrm{K}^+]_\mathrm{CP}$ | $[\mathrm{K}^+]_\mathrm{B} = 4$ | mM |
| $[\mathrm{Na}^+]$ | - | $[\mathrm{Na}^+]_\mathrm{CP}$ | $[\mathrm{Na}^+]_\mathrm{B} = 144$ | mM |
| $[\mathrm{Cl}-]$ | - | $[\mathrm{Cl}-]_\mathrm{CP}$ | $[\mathrm{Cl}-]_\mathrm{B} = 130$ | mM |
| $[\mathrm{L}]$ | - | $[\mathrm{L}]$ | - | mM |
| $[\mathrm{KL}]$ | - | $[\mathrm{KL}]$ | - | mM |
| $p$ | $p_\mathrm{M} = 97.97$ | $p$ | - | M |

‡ $p_\mathrm{M}$ assumed from the concentration of free electrons in gold, i.e, $5.9 \cdot 10^{28}$ m$^{-3}$.

In the model equations considered in this study there are 8 free variables to solve: $\psi_c$, $\psi_p$, $[K^+]_{CP}$, $[Na^+]_{CP}$, $[Cl^-]_{CP}$, [L], [KL], $p$. From the assumptions i), ii), iii), and iv) follow the below Eqs. S5.a-b), c-f), g), and h), respectively.

$$[K^+]_{CP} + [Na^+]_{CP} - [Cl^-]_{CP} + p - [PSS^-] + [KL] = 0 \tag{S10a}$$

$$p - \frac{C_V}{F}(\psi_p - \psi_c) = 0 \tag{S10b}$$

$$[K^+]_{CP} - [K^+]_B \exp\left(-\frac{F\psi_c}{RT}\right) = 0 \tag{S10c}$$

$$[Na^+]_{CP} - [Na^+]_B \exp\left(-\frac{F\psi_c}{RT}\right) = 0 \tag{S10d}$$

$$[Cl^-]_{CP} - [Cl^-]_B \exp\left(\frac{F\psi_c}{RT}\right) = 0 \tag{S10e}$$

$$p - p_M \exp\left(\frac{F}{RT}(V_{app,0} - \psi_p)\right) = 0 \tag{S10f}$$

$$[KL] - \beta_{KL}[K^+]_{CP}[L] = 0 \tag{S10g}$$

$$[L] + [KL] - [L]_{tot} = 0 \tag{S10h}$$

**ionoCP release**: this study analyzes the concentration change of potassium ions in the ECF at equilibrium based on the final value of the applied stimulus at the metal contact, $\psi_{p,M} = V_{app,max}$. Therefore, the model uses the solution obtained with the pre-charging study (see above) as initial conditions for concentrations of potassium ions (free and complexed indicated as $[K^+]_{CP,0}$ and $[LK]_0$ in the following) and enforces mass conservation of these ions using fixed CP and ECF volumes. This model has therefore 9 unknown variables to solve: the 8 of the previous study plus $[K^+]_{ECF}$:

$$[K^+]_{CP} + [Na^+]_{CP} - [Cl^-]_{CP} + p - [PSS^-] + [KL] = 0 \tag{S11a}$$

$$p - \frac{C_V}{F}(\psi_p - \psi_c) = 0 \tag{S11b}$$

$$[K^+]_{CP} - [K^+] \exp\left(-\frac{F\psi_c}{RT}\right) = 0 \tag{S11c}$$

$$[Na^+]_{CP} - [Na^+]_B \exp\left(-\frac{F\psi_c}{RT}\right) = 0 \tag{S11d}$$

$$[Cl^-]_{CP} - [Cl^-]_B \exp\left(\frac{F\psi_c}{RT}\right) = 0 \tag{S11e}$$

$$p - p_M \exp\left(\frac{F}{RT}(V_{app,max} - \psi_p)\right) = 0 \tag{S11f}$$

$$[KL] - \beta_{KL}[K^+]_{CP}[L] = 0 \tag{S11g}$$

$$[L] + [KL] - [L]_{tot} = 0 \tag{S11h}$$

$$([K^+]_{CP} + [LK] - [K^+]_{CP,0} - [LK]_0)V_{CP} + ([K^+] - [K^+]_B)V_{ECF} = 0, \tag{S11i}$$

where $V_{CP}$ and $V_{ECF}$ are the volumes of the CP and the ECF, respectively.

**Compartments volume**: while $V_{CP}$ is given by the adopted geometry (see Table S5), the value used for $V_{ECF}$ must reflect the dynamics of the ionic actuator, namely the

ion diffusion space around the CP for a given time interval. In fact, this optimization tool provides an estimate on the total modulation at $t = \infty$ while the ionoCP operates in dynamic conditions. Thus, one way to exploit the results of the simplified model is to assume an effective volume that is actually modulated during the ion release, before ions disperse in the bulk of ECF. In this paper, based on the results presented in the main body, we used an interval $\Delta t = 150$ ms and considered the ECF volume as the 3D space within $\sqrt{D_{\mathrm{K}}\Delta t}$ all around the CP, and subtracted the volume occupied by the neuron cell.

**Solver**: Solutions of Eqs. (S10) and (S11) were found developing an *ad-hoc* Newton-Raphson solver. Parameters such as $\beta_{\mathrm{KL}}$, $[\mathrm{PSS}^-]$, $[\mathrm{L}]_{\mathrm{tot}}$, $V_{\mathrm{app,max}}$ were varied according to the optimization process as described in the main body.

# References


[1] J. R. Cressman, G. Ullah, J. Ziburkus, S. J. Schiff, and E. Barreto, "The influence of sodium and potassium dynamics on excitability, seizures, and the stability of persistent states: I. single neuron dynamics," *Journal of computational neuroscience*, vol. 26, no. 2, pp. 159–170, 2009. DOI: 10.1007/s10827-008-0132-4.

[2] M. O. Bamgbopa, J. Edberg, I. Engquist, M. Berggren, and K. Tybrandt, "Understanding the characteristics of conducting polymer-redox biopolymer supercapacitors," *Journal of Materials Chemistry A*, vol. 7, no. 41, pp. 23 973–23 980, 2019. DOI: 10.1039/c9ta07030c.

[3] A. J. Bard, L. R. Faulkner, and H. S. White, *Electrochemical methods: fundamentals and applications*, 2nd ed. John Wiley & Sons Inc., 2001, ISBN: 9780471043720.

[4] K. Tybrandt, I. V. Zozoulenko, and M. Berggren, "Chemical potential–electric double layer coupling in conjugated polymer–polyelectrolyte blends," *Science advances*, vol. 3, no. 12, eaao3659, 2017. DOI: 10.1126/sciadv.aao3659.

[5] J. Rivnay, P. Leleux, M. Ferro, *et al.*, "High-performance transistors for bioelectronics through tuning of channel thickness," *Science Advances*, vol. 1, no. 4, pp. 1–6, 2015. DOI: 10.1126/sciadv.1400251.

[6] J. J. Jasielec, T. Sokalski, R. Filipek, and A. Lewenstam, "Neutral-Carrier Ion-Selective Electrodes Assessed by the Nernst-Planck-Poisson Model," *Analytical Chemistry*, vol. 87, no. 17, 2015. DOI: 10.1021/acs.analchem.5b00065.

[7] M. J. Sætra, G. T. Einevoll, and G. Halnes, "An electrodiffusive neuron-extracellular-glia model for exploring the genesis of slow potentials in the brain," *PLoS Computational Biology*, vol. 17, no. 7, 2021. DOI: 10.1371/journal.pcbi.1008143.

[8] *Comsol multiphysics user manual*, COMSOL Inc., Sweden, 2022.

[9] J. Pods, J. Schönke, and P. Bastian, "Electrodiffusion models of neurons and extracellular space using the poisson-nernst-planck equations - Numerical simulation of the intra- and extracellular potential for an axon model," *Biophysical Journal*, vol. 105, no. 1, 2013. DOI: 10.1016/j.bpj.2013.05.041.

[10] A. Fellner, A. Heshmat, P. Werginz, and F. Rattay, "A finite element method framework to model extracellular neural stimulation," *Journal of Neural Engineering*, vol. 19, no. 2, p. 022 001, Apr. 2022. DOI: 10.1088/1741-2552/AC6060.

[11] R. Bestel, U. Van Rienen, C. Thielemann, and R. Appali, "Influence of Neuronal Morphology on the Shape of Extracellular Recordings with Microelectrode Arrays: A Finite Element Analysis," *IEEE Transactions on Biomedical Engineering*, vol. 68, no. 4, 2021. DOI: 10.1109/TBME.2020.3026635.